THESIS FOR THE DEGREE OF LICENTIATE OF ENGINEERING IN THERMO AND FLUID DYNAMICS

On Aero Engine Intercooling

XIN ZHAO

Department of Applied Mechanics
CHALMERS UNIVERSITY OF TECHNOLOGY
Gothenburg, Sweden 2013

On Aero Engine Intercooling
XIN ZHAO

Thesis for the degree of Licentiate of Engineering 2013:23
ISSN 1652-8565
Department of Applied Mechanics
Chalmers University of Technology
SE-412 96 Gothenburg
Sweden
Telephone: +46 (0)31-772 1000

Chalmers Reproservice
Gothenburg, Sweden 2013

On Aero Engine Intercooling
Thesis for the degree of Licentiate of Engineering in Thermo And Fluid Dynamics
XIN ZHAO
Department of Applied Mechanics
Chalmers University of Technology

Abstract

Establishing an optimal intercooled aero engine constitutes a coupled problem where the conceptual design of the intercooler and the engine has to be considered simultaneously. The heat transfer and pressure loss characteristics will depend on the choice of the intercooler architecture. Hence, to be able to optimize the performance of an intercooled aero engine, the performance characteristics of a given intercooler architecture has to be known in the parameter range anticipated for the aero engine optimization. In this thesis, several design concepts of a two-pass cross flow tubular intercooler for aero engine application have been analyzed by the use of computational fluid dynamics simulations and system level assessments.

The work comprises 3D coupled CFD analysis of the internal flow (in-flow, cross-over and out-flow duct) using porous media modelling for the tube stacks. Several design iterations on the internal flow configuration has been performed applying two splitter vanes and a flow guide vane. A parametric study of the external heat transfer and pressure loss is included. Correlations for two configurations (straight tube and involute spiral tube) are provided for system level assessments of this intercooler concept. In addition to providing heat transfer and pressure loss characteristics, the correlations are set up to allow intercooler installation space constraints to be taken into account.

The fuel burn benefits of the presented intercooled engine are attributed to the use of a variable geometry separate exhaust nozzle and to providing an adequate amount of intercooling. The amount of intercooling should be sufficient to enable the high OPR at take-off, and allow a compact engine design. In cruise, on the other hand, it is beneficial to reduce the intercooling to establish an optimum between intercooling and incurred pressure losses.

Keywords: intercooler, aero engine, CFD, system performance, porous media, coolant flow control

Acknowledgements

This work is financially supported by the E.U. under the 'LEMCOTEC - Low Emissions Core-Engine Technologies', a Collaborative Project co-funded by the European Commission within the Seventh Framework Programme (2007-2013) under the Grant Agreement 283216.

I would like to firstly express my deep gratitude to my supervisor Professor Tomas Grönstedt for his patient guidance, enthusiastic attitude of research work, and humorous remarks. I am also particularly grateful for the fruitful discussions with Anders Lundbladh from GKN Aerospace, and Andrew Rolt from Rolls-Royce UK, many thanks for your help. Furthermore, special thanks should be given to Lei Xu at Simens now for the initiation of this work, Konstantinos Kyprianidis at Rolls-Royce Defence Aerospace for his contributions to the second paper in this thesis, and Dennis Jacobsson from GKN Aerospace for the help in the LEMCOTEC project.

My special thanks are extended to all my colleagues in the Fluid Dynamics Division for their kind help and the nice working atmosphere.

Nomenclature

Abbreviations

BPR	Bypass ratio
CFD	Computational fluid dynamics
FPR	Fan pressure ratio
HPC	High pressure compressor
HPT	High pressure turbine
IPC	Intermediate pressure compressor
LPT	Low pressure compressor
OPR	Overall pressure ratio
PR	Pressure ratio
SFC	Specific fuel consumption $[mg/N{\cdot}s]$
TET	Turbine entry temperature [K]

Latin symbols

A_c	Minimum flow cross section area of the computational domain $[m^2]$
A_f	Intercooler frontal area of the computational domain $[m^2]$
A_w	Heat transfer wall area of the computational domain $[m^2]$
a	Major axis length of the ellipse $[m]$
b	Minor axis length of the ellipse $[m]$
D	Hydraulic diameter of single elliptical tube $[m]$
D_h	Hydraulic diameter of a tube stack computational domain $[m]$
d_a	Axial spacing between tube columns $[m]$
d_b	Transversal spacing between tube rows $[m]$
f	Friction factor
h	Heat transfer coefficient $[J/(m^2{\cdot}s{\cdot}K)]$
j	Colburn j factor
k_{tube}	Tube internal flow loss coefficient
k'	Darcy pressure loss coefficient for porous media model
L	Total flow length of the intercooler $[m]$
$\dot{m}$	Mass flow rate $[kg/m^3]$
V	Flow Velocity $[m/s]$
Nu	Nusselt number
Pr	Prandtl number
Re	Reynolds number
St	Stanton number
Δp	Pressure drop $[Pa]$

Greek symbols

ρ	Density $[kg/m^3]$
μ	Dynamic Viscosity $[kg/(m \cdot s)]$
η	Efficiency
κ	Thermal conductivity of air $[J/(m \cdot s \cdot K)]$

Thesis

This thesis consists of an extended summary and the following appended papers:

Paper A Zhao, X. and Grönstedt, T., **Conceptual Design of a Two-Pass Cross Flow Aero-Engine Intercooler**. Submitted to Journal of Engineering for Gas Turbine and Power.

Paper B Zhao, X., Grönstedt, T. and Kyprianidis, K., **Assessment of The Performance Potential for a Two-pass Cross Flow Intercooler for Aero Engine Applications**. The 21th ISABE conference, September 9-13, 2013, Busan, South Korea.

Contents

1 Introduction

1.1 Background

As a vital part of the increasingly globalised world economy and cultural exchange, aviation contributes to the growth of international trade, tourism and connects people from different continents. In the foreseeable future, it is estimated that global air traffic will be growing with about 5% per year [1]. If this projection comes true, the world's air traffic is going double by 2030. Besides the economic effect, more attention has been devoted to the environmental concerns which the air traffic growth could bring, and the fuel crisis which it could meet with. To obtain a sustainable future and minimize the impact of the fuel price and shortage, higher efficiency for the aero engines must then be achieved.

From the basic understanding of the Brayton cycle, it is clear that the theoretical thermal efficiency of a gas turbine increases with an increasing overall pressure ratio (OPR), as illustrated in Figure 1.1.1. At the present time, civil aero engines typically operate between OPR 30 and 40, for instance, Rolls-Royce Trent 900 used on Airbus A380 has an OPR around 40 and GE90-94B used on Boeing 777 has an OPR of 39.6. The trend of the newly launched aero engines is a steady increase in OPR. The General Electric GEnx used on Boeing 787 and Airbus A350XWB has an OPR around 43 at take-off and 52 at top of climb and the Rolls-Royce Trent 1000 used on Boeing 787 has an OPR of 47.7 at take-off and 50.0 at the climb phase [2]. Obviously, there is still a considerable efficiency benefit that can be drawn out from pushing the OPR to a higher value.

However, to obtain a higher value of OPR has two major obstacles. Firstly, a high OPR will result in an excessive high pressure compressor (HPC) exit temperature which is primarily limited by the high pressure turbine (HPT) disc and blade cooling requirements. Secondly, the efficiency of the HPC is strongly influenced by the HPC last blade height and hub/tip ratio. When the pressure ratio goes too high, the area needs to be reduced to pass the air with very high density, which means a very short blade height and/or a large hub/tip ratio. For state of the art engines, compression inefficiency related to tip clearance loss and end wall boundary layer loss start to dominate when last stage blade heights goes below approximately 12 mm and the hub/tip ratio is larger than 0.92. Therefore, attention must be taken to these parameters when the engine design is aiming at a very high OPR.

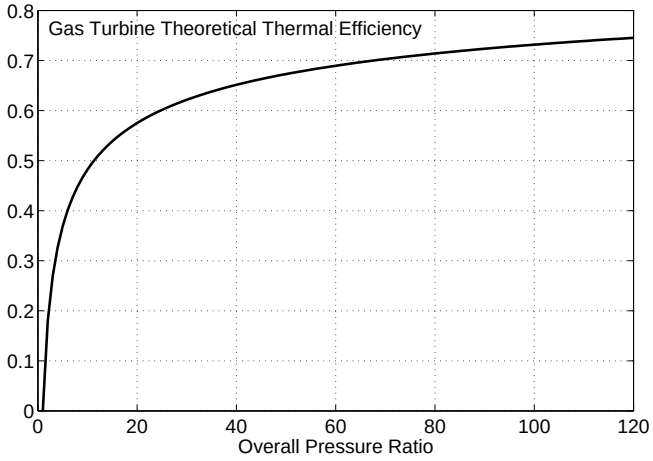

Figure 1.1.1: *Gas turbine theoretical thermal efficiency*

1.2 Rationale of intercooled aero engines

An intercooled cycle, to be found in most thermodynamic and gas turbine textbooks see Figure 1.2.1, is one of the potential technologies enabling high OPRs of aero engines. Actually, intercooling technology has already

been applied to marine gas turbines [3], and stationary engines for electricity generation [4]. By reducing the compressed air temperature, the compression work required can be reduced by allowing an approximate isothermal compression.

For aero engine applications, intercooling may provide more benefits than the reduction of compression work and the enabling of a high OPR. Other advantages provided by intercooling may be a smaller engine core size through increased specific thrust level, a reduced HPT cooling air requirement through reduced cooling air temperatures and reduced NOx emissions through reduced combustor flame temperatures [5, 6, 7, 8, 9, 10]. In addition, with the intercooling technology, one can choose to increase the combustor exit temperature while increasing the OPR in a balanced way to optimize the efficiency. To increase the combustor exit temperature is another way to take benefit of the reduced temperature of the cooling air [11].

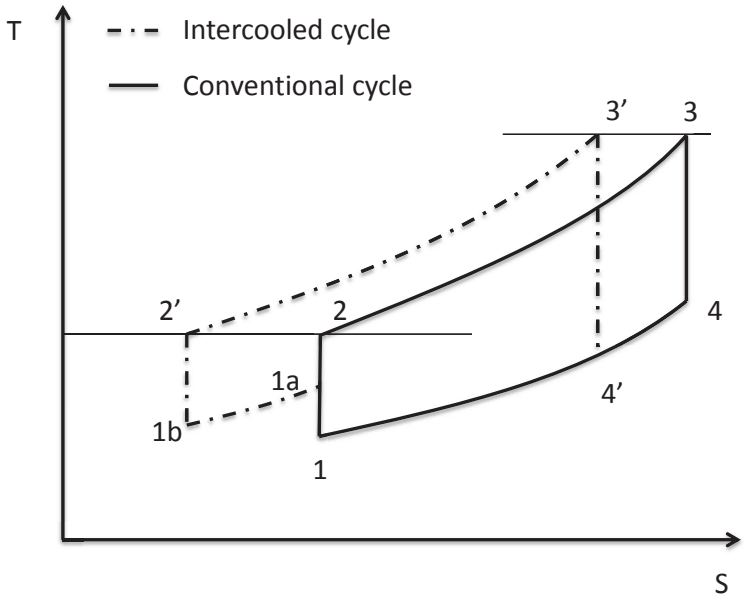

Figure 1.2.1: *Intercooled cycle*

1.3 Pathways to good intercooled aero engines

Establishing an optimal intercooled aero engine constitutes a coupled problem where the conceptual design of the intercooler and the engine has to be considered simultaneously. The heat transfer and pressure loss characteristics will depend on the choice of the intercooler architecture. Hence, to be able to optimize the performance of an intercooled aero engine, the performance characteristics of a given intercooler architecture has to be known in the parameter range anticipated for the aero engine optimization. Although the design of compact heat exchangers is a mature field and a wealth of design data exists [12], the availability of data directly applicable to aero engine performance studies is quite limited. In chapter 2, the conceptual design of a tubular two-pass cross flow intercooler architecture intended for a turbofan aero engine application is presented.

Unlike the intercooled stationary gas turbines, which allow the use of a bulky intercooler installation, it is particularly important to achieve a compact intercooler design for aero engine applications. Increasing the volume requirement may lead to an increase in maximum engine diameter and add to installation losses through nacelle drag. Increased volume may also negatively influence pressure losses associated with the intercooler installation, add to shaft lengths and in turn cause vibration problems. Additionally, increased engine weight will offset the fuel burn benefits from improved SFC. Hence, at the same time of delivering adequate heat transfer at a sufficiently low pressure loss, attention must be paid to the intercooler weight and volume size.

As mentioned above, an optimal intercooled engine has to consider not only the intercooler itself, but also how

to integrate the intercooler into the engine. Within this work it is argued that it is beneficial to provide a sufficient amount of intercooling at take-off to allow for a compact engine design with a high OPR and a reduced cooling flow need. In cruise, on the other hand, it is beneficial to reduce the intercooling to establish an optimum between intercooling and incurred pressure losses. To achieve this control, the intercooler may be integrated either allowing the internal bypass air to mix with the external bypass air using a variable mixer geometry, see upper part of Figure 1.3.1, or to be exhausted separately as indicated in the lower part of Figure 1.3.1, by using a variable geometry nozzle.

Another design issue that has to be addressed is to decide where in the compression process the intercooling should be introduced. An intercooler may be integrated anywhere in the compression process downstream of the fan, but positioning it too early will reduce the performance primarily through pressure loss and weight penalties, and positioning it too late will not be favorable from a thermodynamic perspective. Engine architectures suitable for integration would be three-shaft and geared concepts which can be designed with a relatively high pressure ratio on the upstream compressor. A geared fan intercooled engine is adopted in this thesis and the design strategy will be discussed further as part of the engine performance analysis presented in chapter 3.

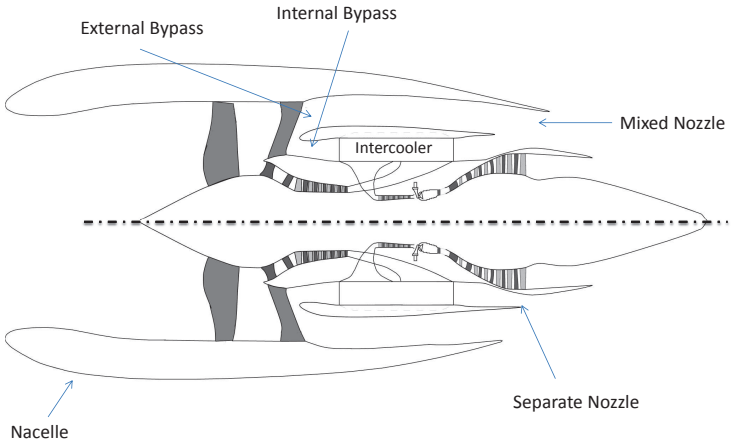

Figure 1.3.1: *Intercooled engine arrangement with two-pass cross flow configuration [13].*

2 Two-pass tubular intercooler design

The two-pass cross flow tubular intercooler is configured between the IPC and the HPC as shown in Figure 1.3.1. As illustrated in Figure 2.0.1 below, flow exiting an intermediate compressor or high speed booster enters the inflow duct through which it is diffused. The flow then enters the first stack of a tubular heat exchanger located downstream in the cooling flow direction, returns to an upstream tubular heat exchanger and then continues to an accelerating duct leading to the high pressure compressor entrance. Bypass air flows over the external surfaces of the two tube stacks to achieve the sought intercooling.

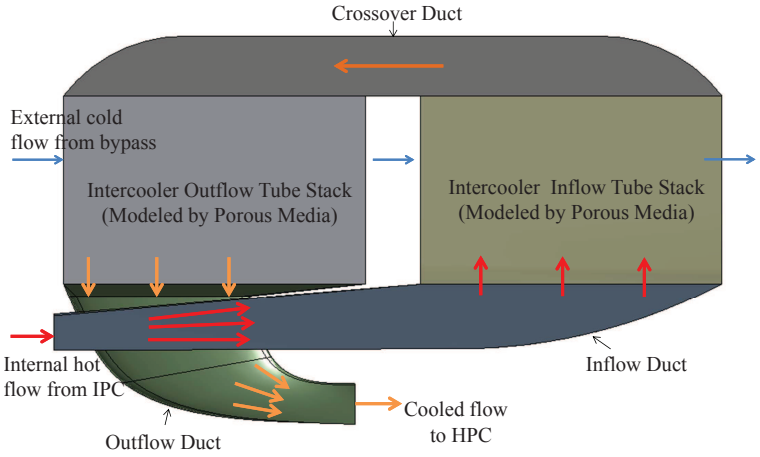

Figure 2.0.1: *Layout of the two-pass cross flow intercooler concept*

2.1 Tube configurations

Three different configurations for the two-pass cross flow intercooler have been evaluated. The straight tube configuration (Figure 2.1.1) was firstly introduced and studied, followed by the involute spiral (Figure 2.1.2) and the U-bent involute spiral (Figure 2.1.3) configurations applying the same study strategy. The latter configuration is hereafter simply referred to as the U-bent configuration.

2.1.1 Straight configuration

The straight tube configuration has the simplest geometry which, however, gives the lowest space utilization as illustrated in Figure 2.1.1. Due to the space wasted between tube stacks, the straight tube configuration ended up with a relatively large intercooler, and a small frontal area which leads to a high inflow velocity and a high pressure loss. Nevertheless, the study of the straight tube configuration gave valuable experience in designing the connecting ducts and tube stacks.

2.1.2 Involute spiral configuration

The involute spiral concept, as shown in Figure 2.1.2, is developed to provide a better space utilization in comparison with the straight tube configuration. The tubes are bent following an involute spiral track which can be designed to almost completely occupy the space where the tubes extend. With this improvement in space utilization one can choose to reduce the length of the intercooler in the axial or/and the radial direction, to decrease installation volume required and/or to reduce the incurred pressure loss.

Comparing to the straight tube, the bent tube is also considered having a higher heat transfer and loss coefficient due to secondary flow effects. However, this effect for the involute spiral tubes is not quantified in any

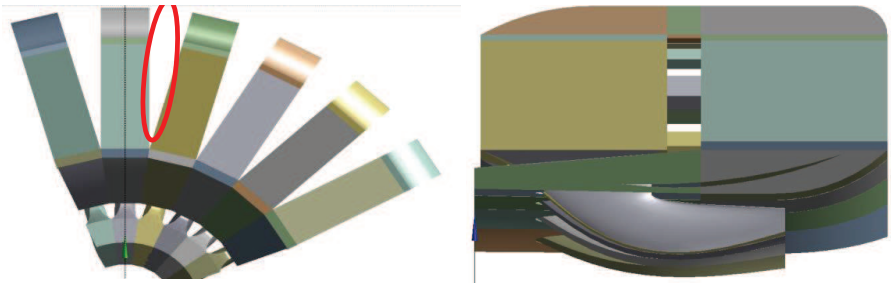

Figure 2.1.1: *Straight tube configuration*

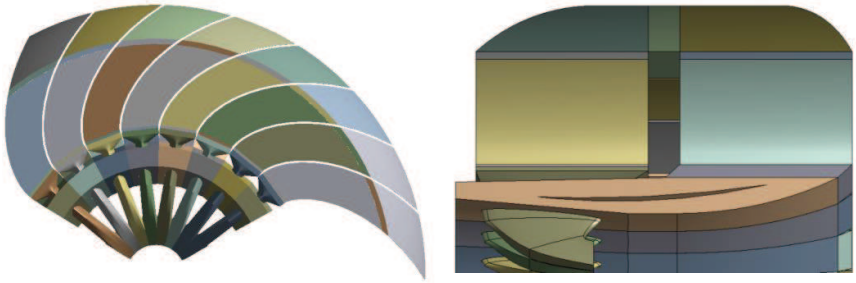

Figure 2.1.2: *Involute spiral tube configuration*

published correlations [14, 15]. Therefore, CFD simulations were carried out to estimate the flow and heat transfer characteristics of this configuration.

2.1.3 U-bent configuration

The U-bent tube configuration creates a part of a counter flow pass which could increase heat transfer capability compared to the cross flow pass. As shown in Figure 2.1.3, the crossover duct is replaced by a direct tube-to-tube connection, which leads to a more efficient space utilization. Without the crossover duct, the losses incurred by the sudden exit (tube stack to duct) and the sudden entry (duct to tube stack) can be reduced. However, the initial study shows that the flow mal-distribution of this concept is relatively severe because the length of the tubes varies substantially. One solution to this could be to use a varying tube diameter to offset the effect. This has been evaluated and good results have been obtained.

2.2 External side - basic arrangement of intercooler tubes

On the external side of the two-pass cross flow intercooler, the pressure loss incurred over the tubes is necessary to generate the heat transfer. A trade-off between heat transfer and pressure loss must be established in order

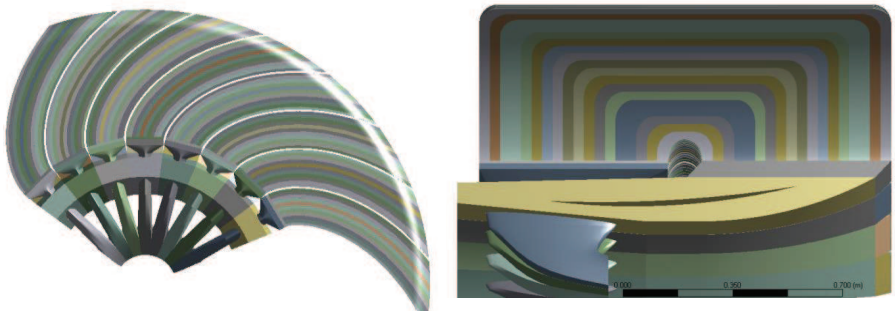

Figure 2.1.3: *U-bent tube configuration*

to determine the optimal intercooler design. Going to higher levels of pressure loss has the drawback that fluid acceleration due to reduced stagnation pressure and heat addition tend to drive the loss levels up quickly for a relatively modest gain in heat transfer, while lower pressure loss levels require excessive volume or tend to make the heat transfer insufficient.

Elliptical shape tubes with an aspect ratio of 8.0 are selected, which gives almost twice the external heat transfer area (perimeter $\times$ tube length) compared to a circular tube geometry having the same cross sectional area. As presented in [16], the heat transfer capability of elliptical cylinders increases rapidly from an aspect ratio around two to up to around eight after which there is only a limited improvement. Elliptic shaped tubes run the risk of deformation due to the pressure difference between the internal and the external sides. However, it is believed that the suggested tube geometry can be produced in such a way that it will maintain its shape during operation. A manufacturing process for this type of tube is described in [17].

Apart from the aerodynamic shape of a single tube, the effect of different tube arrangements, in terms of inter-tube spacing, also needs to be explored. A number of two-dimensional simulations have been performed for establishing pressure loss and heat transfer characteristics of the external cold side. A schematic sketch of the problem configuration and an overview of the computational domain are shown in Figure 2.2.1. The range for d_a and d_b parameters are given in Table 2.2.1. A more extensive parameter range has been explored but this data set covers the solution space where the most favorable configurations have been detected. Going above n=1 or m=3 generally reduces intercooler performance by increasing size, volume and weight. Below n=0.75 and m=1.0 it is difficult to achieve low losses for the relatively large mass flow needed to obtain a sufficient amount of exchanged heat.

Distance along the external side flow direction $d_a = n \cdot a$	$n = 0.75, 0.8786, 1$
Distance along the transversal direction $d_b = m \cdot b$	$m = 1, 2, 3$
Ellipse aspect ratio	$a/b = 8/1$
Temperature at the wall	$556\ K$
Inlet flow Mach number	$0.05 - 0.2$
Inlet flow temperature	$349\ K$
Outlet pressure	$1\ bar$

Table 2.2.1: Intercooler external side parameter range and boundary conditions

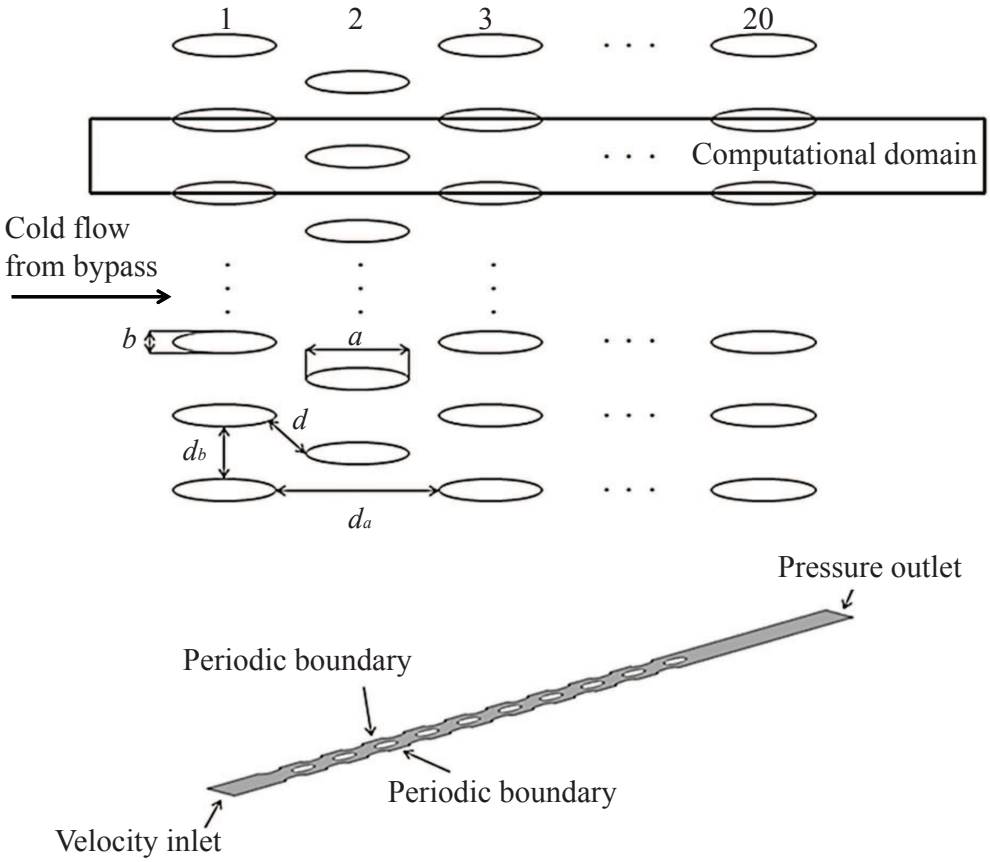

Figure 2.2.1: *Intercooler external side computational domain*

For the evaluation of the heat transfer and aerodynamic properties of the external side of the intercooler, the dimensionless heat transfer coefficient, the Colburn j factor, is introduced [12]:

$$j = St \cdot Pr^{2/3} = \frac{Nu}{Re \cdot Pr} \cdot Pr^{2/3} \tag{2.2.1}$$

The Nusselt number, the Reynolds number of the flow field and related hydraulic diameter are calculated from the expressions suggested by Kays and London [12]:

$$D_h = \frac{4A_cL}{A_w} \; ; \quad Nu = \frac{hD_h}{\kappa} \; ; \quad Re = \frac{(\dot{m}/A_c) \cdot D_h}{\mu} \tag{2.2.2}$$

where h is the local heat transfer coefficient; D_h is the hydraulic diameter of the flow field; k is the thermal conductivity of air; A_w is the surface area of the ellipses; A_c is the minimum flow cross sectional area and L is the total flow length of the intercooler. The friction factor f is defined through [12]:

$$\Delta p = \frac{(\dot{m}/A_c)^2}{2\rho_i}[f\frac{A_w}{A_c}\frac{\rho_i}{\rho_m} + (1+\sigma^2)(\frac{\rho_i}{\rho_o} - 1)] \tag{2.2.3}$$

where ρ_i and ρ_o are the fluid inlet and outlet density, ρ_m is the average of ρ_i and ρ_o, σ is the ratio between the minimum flow cross sectional area A_c and the intercooler frontal area A_f, and $\dot{m}$ is the mass flow at the inlet. In this equation the friction factor f represents an equivalent shear force per unit area in the flow direction composed of the true viscous shear forces as well as the pressure forces.

2.2.1 External side CFD settings

The data given in Table 2.2.1 represents the boundary conditions used in the parametric study of the external side. The inlet flow Mach number is varied to establish correlations in the average flow field Reynolds number range $10,000 < Re < 120,000$. This range covers the anticipated range for all the mission points to be studied.

To resolve the boundary layers around the elliptical tubes, the meshes were generated to get $y^+ < 1$. A mesh independency study was performed to establish the final mesh settings to be used for all the cases. Three hybrid meshes which have a maximum face size of 0.4 mm, 0.3 mm, 0.2 mm, resulting in around 0.7 million, 1.0 million and 1.7 million elements respectively have been compared. The results show that the relative deviation in stagnation pressure between the 0.7 million and 1.0 million cases was around 2% and the difference between the 1.0 million and 1.7 million was 0.6%. To achieve a reasonably accurate result without excessive computation time, the 1.7 million elements mesh was considered sufficient. The computations have been performed using CFX. The shear stress transport (SST) turbulence model is adopted here, which has shown to give reasonably good predictions of separation and possible flow recirculation modelling [18, 19].

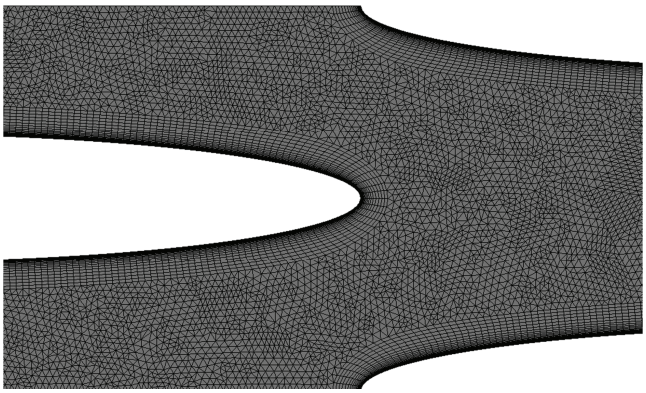

Figure 2.2.2: *2D hybrid mesh for the external side simulations*

2.2.2 External side results

After some initial screening three cases with transversal distances $d_b = b$, $d_b = 2b$ and $d_b = 3b$, see Figure 2.2.1, were selected as a basis for the analysis. The three cases are denoted A, B and C respectively, and are illustrated schematically in the top of Figure 2.2.3. As will be discussed, case A and case C represent less favourable conditions whereas the case B represent a configuration with good friction and heat transfer characteristics.

Results of case A, B, and C are shown in Figure 2.2.3. For a given average Reynolds number the Colburn j factor and friction factor f generally show an increasing trend with increasing spacing d_b. This is consistent with the general trends that have been observed for circular tube stacks by for instance Kays and London [12].

However, in the high Reynolds number region of case A, the friction factor increases rapidly with increasing Reynolds number and the last point almost meets the curve of case C. In case A, the tube passage form convergent divergent ducts, with an area ratio considerably larger than in case B and C. As the Mach number increases through the tube array, it reaches a relatively high value entering the last tube column. The small area, increase in stagnation temperature and reduction of stagnation pressure cause the flow to choke in the smallest passage, and then accelerate further into the divergent part where a shock occurs, see Figure 2.2.4.

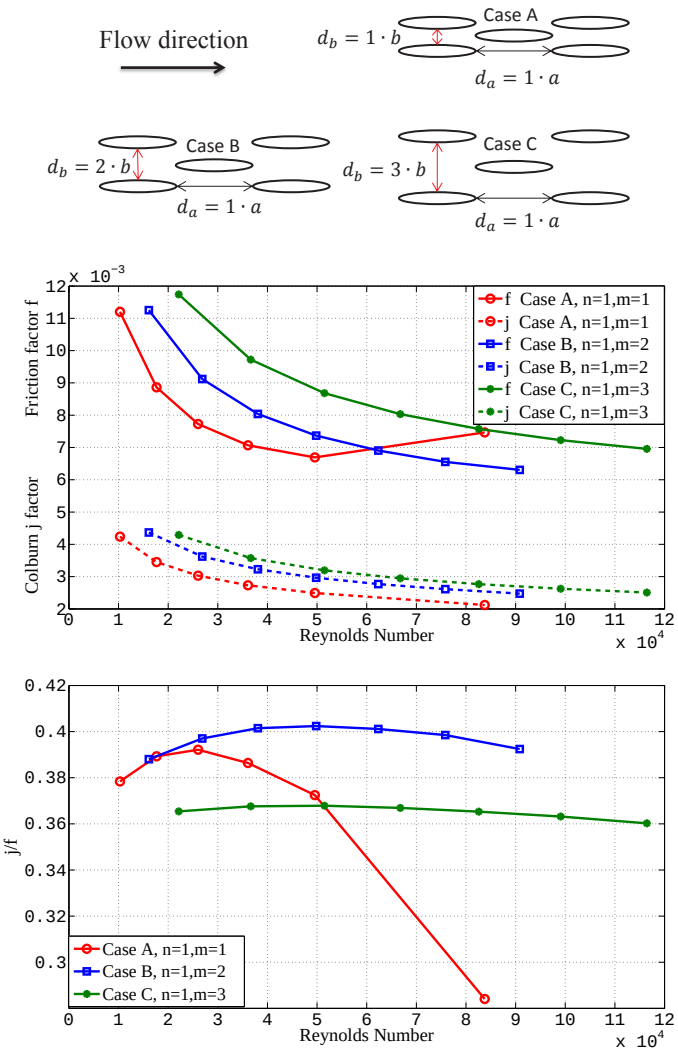

Figure 2.2.3: *For the cases with varying d_b: Colburn j factor and friction factor f (Top). Ratio between j and f (Bottom)*

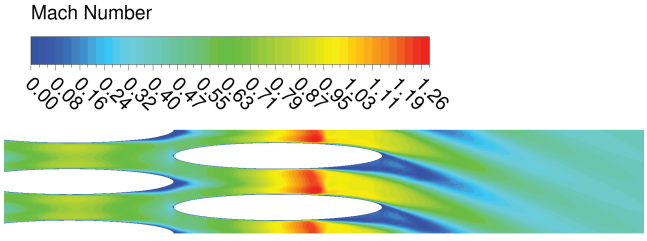

Figure 2.2.4: *Shock wave and asymmetric separation [20] for the last tube column, (Case A, $n = 1, m = 1$)*

The calculated ratio of the Colburn j factor to the friction coefficient f, as shown in the lower part of Figure 2.2.3, gives a considerably higher ratio for case B than for case C. On average an almost 10% increase in Colburn factor to friction coefficient ratio is observed. Note that case B, having a smaller transversal spacing than case C, also has the advantage of reducing the volume requirement for the intercooler. Case B is therefore selected as a starting point for the analysis of the axial spacing parameter d_a, as presented below.

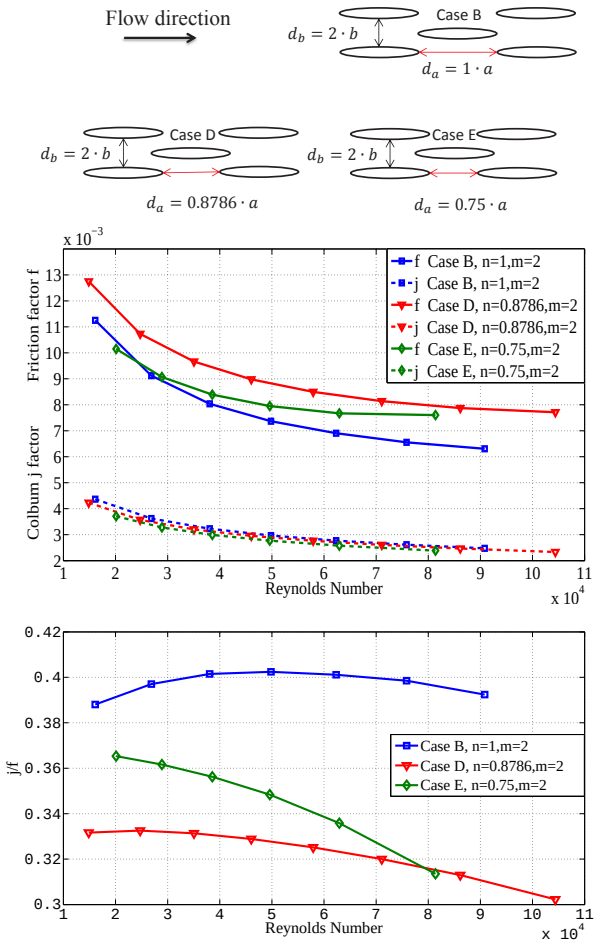

Figure 2.2.5: *For the cases with varying d_a:Colburn j factor and friction factor f (Top) , Ratio between j and f (Bottom)*

For analyzing the effect of varying axial spacing, three cases are selected based on the tube ellipse major axis a having $d_a = a$, $d_a = 0.8786a$ and $d_a = 0.75a$ as illustrated in Figure 2.2.5. These cases are labelled B, D and E respectively, where case B was introduced already as part of the previous section. The value of n in case D (0.8786) is the particular case where the two minimum free-flow areas in flow passage over the ellipse are equal, $d_b = 2d$, as illustrated in Figure 2.2.1. This particular case is selected with the intent to keep the flow path area variation minimal.

The axial spacing parametric study generally shows a greater complexity than observed for the transversal cases. With a smaller axial spacing d_a, as represented by case D in Figure 2.2.5, a higher friction factor than for case B is observed but no significant difference in the Colburn j factor is noted. However, for an even smaller axial spacing the friction factor drops back as seen in case E, although in the high Reynolds number region the friction factor tends to be as high as case D, whereas the heat transfer coefficient is actually somewhat lower. The reason for the unexpected drop in friction factor, as the distance is reduced further from case D to case E, is that the adjacent ellipses start to overlap and create local acceleration/deceleration zones. This is seen from the Mach number contours in Figure 2.2.6. The local acceleration zones suppress boundary layer growth and increase skin friction locally. However the rapid growth of the boundary layer in the retardation zone over the top of the ellipse reduces skin friction over a large part of the surface. Overall this results in a reduction in the friction drag. However, the pressure drag is strongly affected by the rear acceleration zone which creates a low pressure area. Hence the pressure drag of case E will grow more strongly with Reynolds number than for the two other cases and this effect will dominate for a sufficiently large Re-number. For a sufficiently low Re-number case E shows the lowest skin friction and heat transfer coefficient.

The optimal choice on geometry parameters ultimately depends on the engine requirements and can not be

decided at the intercooler component level. The five cases studied above, may have their own benefits in being adopted. Generally, case B is the best option because of the highest ratio between the j factor and f factor, while case D and case E may be preferable when the volume is the most critical requirement. Case A can also be applied in the condition when a low inlet Mach number is achieved.

The flow and heat transfer characteristics, in terms of Colburn j factor and friction factor f, for all the five cases have been established and transferred to a Chalmers in-house performance code $'GESTPAN'$ allowing the optimization of the intercooler parameters together with the engine performance optimization [21].

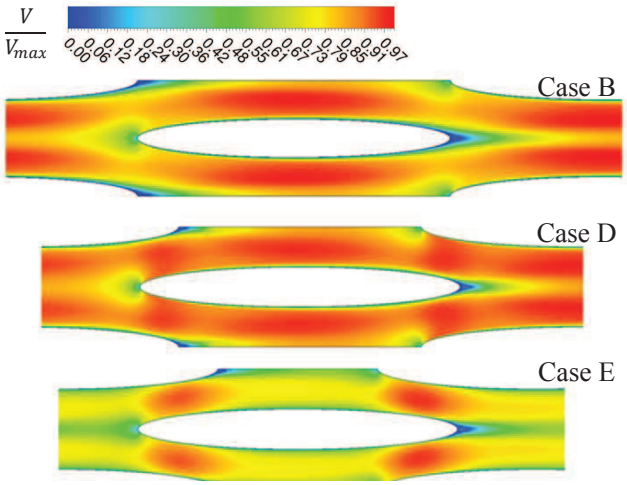

Figure 2.2.6: *Mach number variation around the* 18^{th} *tube column at inflow Mach number of 0.2, Case B (Top), Case D (Middle) and Case E (Bottom)*

2.3 Internal side - connecting ducts design

Walker et al. [22, 23] have, in their experimental and computational work on developing a ducting system for a single pass corrugated intercooler, summarized what the desired internal ducting system must provide to work satisfactorily; a low aerodynamic loss combined with a uniform flow distribution through the heat transfer units in order to achieve a high cooling effectiveness.

On the internal side of the intercooler studied here, the connecting ducts incur a considerable part of the total pressure loss while their contribution to heat transfer is negligible. Previous studies reported for this two-pass cross flow configuration[13, 24] applied correlation based methods for assessing the performance of the connecting ducts. These correlations were based on simplified and general duct geometries which were not able to fully capture the performance of the intercooler installation. Any pressure loss not directly involved in generating heat transfer should be minimized and great care has therefore been taken to minimize the losses occurring in the connecting ducts. Moreover, the flow distribution through the tubes should be considered as an important criterion for the connecting ducts design.

2.3.1 Porous media method

The introduction of a porous media model for calculating properties of the internal side intercooler tube stacks allows realistic loss modelling when calibrated. The advantage is that the entire intercooler can be treated in a single three-dimensional simulation allowing interactions between the connection ducts and the intercooler tubes to be studied, with an affordable computational effort. Missirlis et al. [25, 26, 27] has shown that, without the need for details of the flow in the tube stacks, porous media can sufficiently describe the macroscopic behavior of the heat exchanger. This is a quite valuable approach since the pressure losses in the intercooler tubes strongly influence the flow distribution in the connection tubes and conversely any flow mal-distribution will have a strong effect on the pressure loss distribution in the intercooler tubes. With the tube spacing determined from the external flow modelling, the properties of the porous media can be established.

The porous media simulations are based on the Darcy pressure drop law, set up with a directional pressure loss model. The stream-wise directional loss is determined by the quadratic resistance coefficient k', see [28], defined as:

$$\frac{\Delta p}{\Delta x} = -k' V|V| \tag{2.3.1}$$

where V is the true velocity of the flow assuming an even flow distribution, and Δp is the pressure loss along tube with length Δx. To keep the stream-wise direction as the unique flow direction, the transverse directional loss coefficient is increased typically by a factor of 100 or more to force the flow to follow the direction of the tubes.

Straight tubes characteristics

As a first estimate for the resistance coefficient of the porous media model a correlation for straight circular pipes, as given by Haaland [29], is used:

$$\frac{1}{\sqrt{k_{tube}}} = -1.8 \log_{10}(6.9/Re + (\epsilon/D/3.7)^{1.11}) \tag{2.3.2}$$

where D is the hydraulic diameter of the elliptical tube; ϵ is the roughness of the tube wall, the value of 0.002 mm is assumed here; and Re is the Reynolds number of the internal flow based on the hydraulic diameter of the elliptical tube.

Involute spiral tubes characteristics

For the involute spiral configuration and U-bent configuration, CFD simulations were used to establish the flow and heat transfer characteristics for the internal side of the tubes. As shown in Figure 2.3.1, the bending of the tube introduces a centrifugal force which creates a secondary flow.

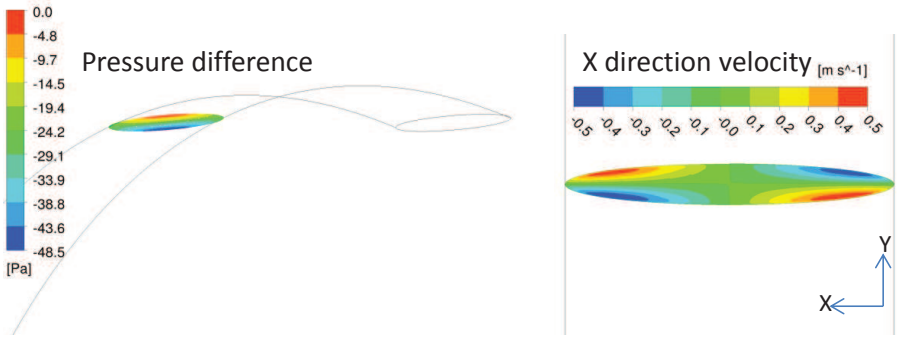

Figure 2.3.1: *Secondary flow effect of the involute spiral elliptical tube*

This secondary flow increases both the friction and heat transfer of the internal side of the involute spiral tube. However, since the heat flux is primarily limited by external heat transfer the benefit from the additional heat transfer is not compensated for by the increased pressure loss. Hence, this normally advantageous effect is not improving the design for this particular configuration.

2.3.2 Connecting ducts

As illustrated in Figure 2.0.1 the inflow duct is connected to the IPC exit and the outflow duct to the HPC entrance. Typical Mach number ranges for these are 0.25-0.35 and 0.45-0.55 respectively [30]. From the inflow duct entrance up to the tube stack, diffusion is needed to provide a flow speed adequate for the inflow tube stack.

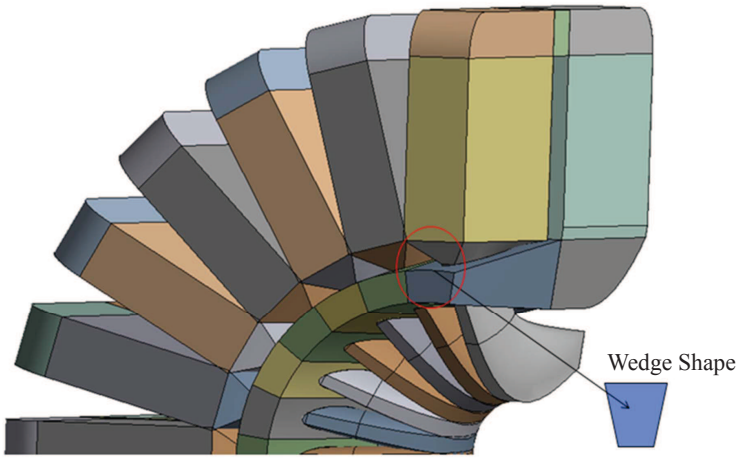

Figure 2.3.2: *Intercooler installation (straight tube configuration side view)*

As will be seen, this diffusion is quite challenging to achieve and this requirement lead to the introduction of guide vanes in the inflow duct.

The internal side simulations are concentrated on a parametric study of the connecting ducts which, to the greatest possible extent, should distribute the flow into the intercooler tubes evenly with an associated low pressure loss. Due to the wedge shaped high speed entry condition, see Figure 2.3.2, and intersection between the inflow duct and the outflow duct, see Figure 2.3.3, a large area variation occurs in both the inflow and outflow ducts which may lead to high pressure losses. Hence, an elliptical shaped outflow duct is designed which crosses through the middle of the inflow duct achieving a smooth area variation in the inflow duct. Initial work on an inflow, outflow configuration with the two ducts passing asymmetrically was carried out. It was found difficult to keep the losses down in the diffusing inflow duct and this concept was therefore abandoned.

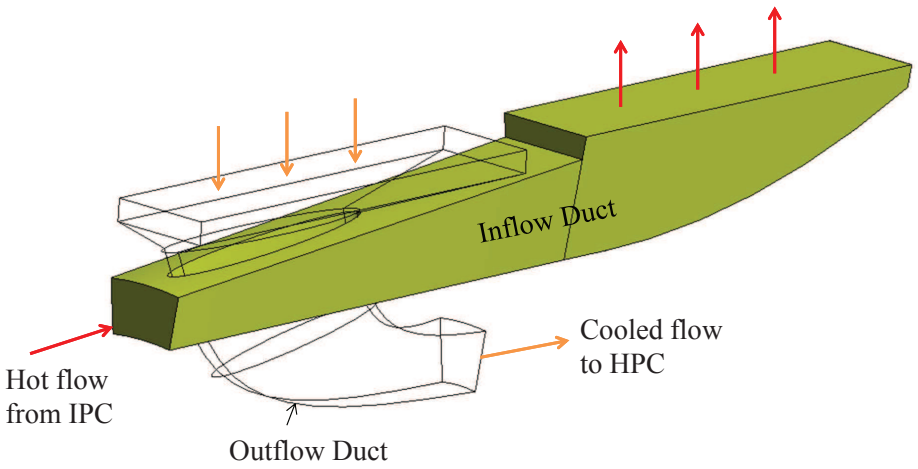

Figure 2.3.3: *Intersection between inflow duct and outflow duct*

2.3.3 Sudden entry and exit

At the interfaces connecting the porous media domain and ducts, a sudden change in porosity occurs which means a sudden change in pressure and velocity, resulting in some pressure losses and possible numerical instability. In reality, a sudden area change, in terms of sudden contraction or sudden expansion, gives rise to considerable pressure losses due to separation, which is particularly pronounced in the sudden expansion case. The loss in

a contracting flow is normally attributed to downstream separation and re-attachment. The inlet flow angle has strong influence on the separation/re-attachment mechanism and is hence quite important for the accurate modelling of a sudden contraction.

An estimate of the loss of the sudden contraction and expansion can be obtained from equations below [31]:

$$K_{suddencontraction} \approx 0.42(1 - \frac{d^2}{D^2}) = \frac{\Delta p}{0.5\rho V^2} \tag{2.3.3}$$

$$K_{suddenexpansion} \approx (1 - \frac{d^2}{D^2})^2 = \frac{\Delta p}{0.5\rho V^2} \tag{2.3.4}$$

where d^2/D^2 is the area ratio between the small area and large area, $0.5\rho V^2$ is the dynamic head based on the elliptical tube area and Δp is the pressure loss. In order to model this sudden contraction and sudden expansion effect in the CFD simulations, porous media transition regions are introduced with pressure loss coefficients based on the analytical equations given above.

Note: this implementation is applied on the study of the involute spiral and U-bent configurations, not the straight tube configuration. It was assumed that the transition regions in the straight tube configuration represent a smoothly varying connection between the tubes and ducts, which performs an ideal flow condition without sudden area change. However, it has been concluded that a completely smooth area transition is very difficult to manufacture, and that this way of modelling gives a more realistic estimate of the intercooler performance.

2.3.4 Guide vane and splitters

At the rear part of the divergent inflow duct, separation may occur very early, leading to high pressure losses and a low degree of flow uniformity as seen from Figure 2.3.4. Here, the flow velocity contour of the cross-section A-A of the porous domain represents the flow distribution in the porous media, and the separation can be observed from the streamline plot. The same phenomenon can be seen in the end of the crossover duct as well due to the high pressure at the corner and the boundary layer growth. The heavy flow mal-distribution in the outflow tube stack is a consequence of the original design of the outflow duct.

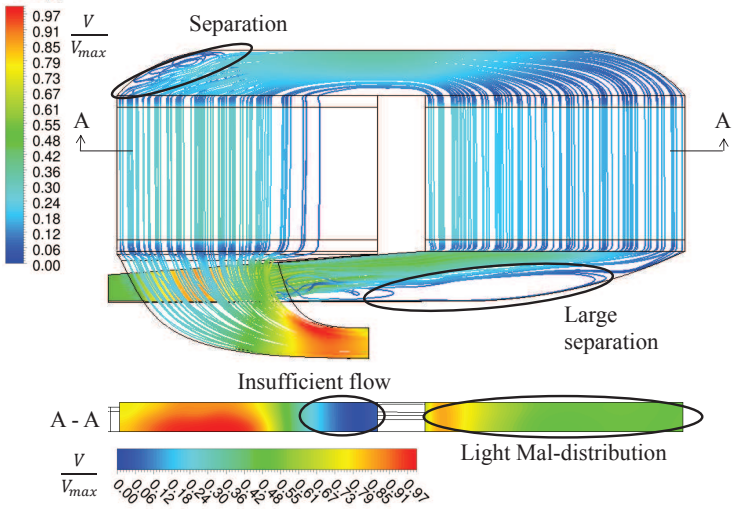

Figure 2.3.4: *Streamline plot of the internal side of the intercooler and velocity contour of the cross-section of the porous media, straight tube configuration without any modification.*

Through the design process of the connecting ducts for the straight tube configuration, several modifications have been introduced based on the original configuration shown above. An aggressive L turn is needed to guide the flow through a 90 degree change of direction. An improved outflow duct configuration is shown in Figure 2.3.5 below. The entry of the 'L' duct is then extended further down in the axial direction to reduce the flow mal-distribution.

The guide vane in the inflow duct, as shown in Figure 2.3.5, is introduced with the purpose to suppress the flow separation and the associated flow mal-distribution and pressure losses. In the crossover duct, there are actually two separations mixed together; one is induced by the upper wall boundary layer growth and the other one is induced by the side wall boundary layer growth. To address this, a guide vane as illustrated in Figure 2.3.5 is applied to eliminate the former separation and a splitter is used to suppress the latter. Splitter 2 in the crossover duct is introduced to help the flow distribution by connecting the rich flow region of the inflow stack directly with the part of the outflow stack receiving insufficient flow. The region with insufficient flow in the outflow stack is indicated in Figure 2.3.4.

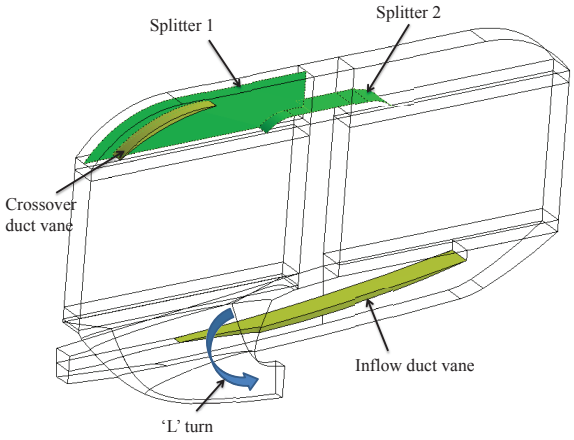

Figure 2.3.5: *Connecting ducts modifications, straight tube configuration*

Similar strategies have also been applied to the design of the connecting ducts for the involute spiral and U-bent concepts.

2.3.5 Pre-deflector

As mentioned in the sudden entry and exit section, pressure losses occur at the interface between the inflow duct and the inflow tube stack, partly due to the sudden area change. In addition, the inlet flow angle can have strong effect on the induced separation of the sudden contraction. Here, a pre-deflector, which is also simulated by porous media modelling, has been introduced to help the flow turning. As a basis for the modelling a parametric CFD study has been performed to estimate the inlet flow angle effect on a single tube geometry. The results are shown in Figure 2.3.6 and Figure 2.3.7. As expected, a smaller inlet flow angle gives lower total pressure loss, while as the inlet flow angle increases, the losses due to the separation will increase.

As described by Ford et al. [32], the porous media simulated vanes are accurate enough to capture the gross fluid behavior. With this intent, a 50 degrees flow turning deflector is installed between the inflow duct and the inflow tube stack, which results in a 40 degrees inlet flow angle. The first guess of the pressure loss coefficient of this deflector is calculated by the Ainley & Mathieson correlation for turbine profile losses [33]. The total loss coefficient for this region then becomes:

$$\Delta p = \frac{\rho v^2}{2}(K_{suddencontraction} + K_{profileloss}) \tag{2.3.5}$$

2.3.6 Internal side CFD settings

Straight tube configuration

For the internal side simulations of the straight tube configuration, a symmetry condition dividing the computational domain into two equal regions was used to reduce the computation effort. The symmetry plane was located in the axial/radial plane.

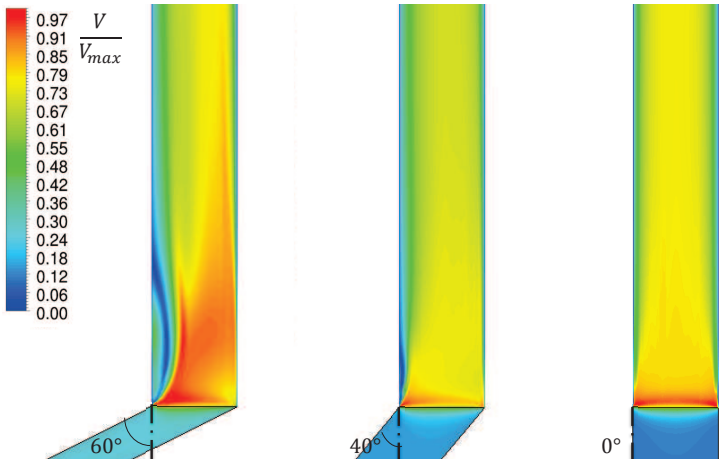

Figure 2.3.6: *Inlet flow angle effect of sudden contraction*

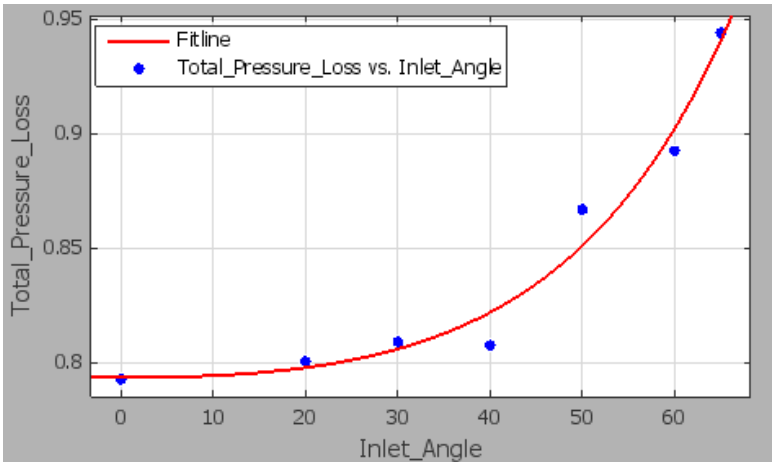

Figure 2.3.7: *Inlet flow angle versus total pressure loss of sudden contraction*

In order to investigate the mesh resolution dependency of the internal hot flow simulation for the straight tube configuration, several meshes were tested. The mesh sizes evaluated are approximately 2 million, 3 million, 4 million, and 6 million elements. Each case was generated with the same meshing strategy. The coarse mesh, 2 million cells, and a refined case, 6 million cells can be seen in Figure 2.3.9. The resulting computational differences using these meshes are relatively modest, showing good consistency with regards to flow separation and flow distribution. To minimize the computational load when simulating different intercooler concepts and operating conditions, the 2 million case was used in the design process and to establish the duct pressure loss correlations, while the 6 million mesh was selected to verify its validity.

A structured mesh is generated in the porous media domain and an unstructured mesh is applied to the ducts. The value of y^+ is less than 200 in the 2 million mesh case, and the automatic wall function in CFX SST model is applied. The boundary conditions are given in Table 2.3.1. These conditions represent the engine operation at take-off which is the most demanding operating condition of the intercooler in terms of heat transfer. The outlet pressure is selected by matching the given mass flow 3.45 kg/s per intercooler module. At top of climb and mid cruise, the mass flows and transferred heat are substantially lower, but so is the density, giving relatively modest variations in flow Mach numbers.

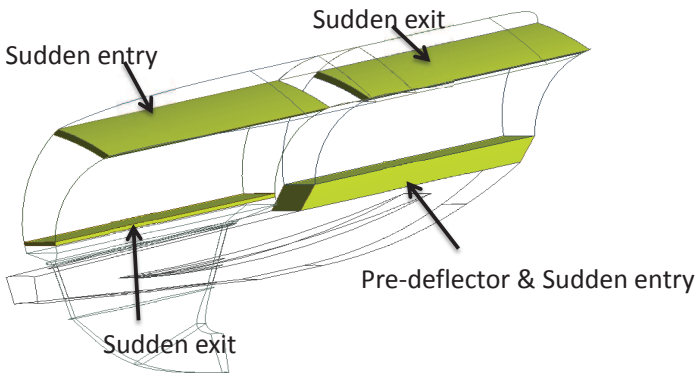

Figure 2.3.8: *Pre-deflector for the involute spiral configuration*

	Boundary Condition Type	Boundary
Inlet	Total Pressure	706 kPa
Inlet	Total Temperature	556 K
Outlet	Pressure	610 kPa
Porous Media	Porosity	0.242
	Stream-wise directional quadratic resistance coefficient k'	8.5 kg/m^4
	Transverse directional loss multiplier	100

Table 2.3.1: Boundary conditions applied to the internal side simulations, take-off operating point

Involute spiral and U-bent configuration

Due to the tubes being bent, the flow in the crossover duct of the involute spiral concept becomes more complex. The symmetry condition will no longer apply and full size simulations need to be conducted. The meshes for these two configurations are shown in the Figure 2.3.10 below.

A mesh sensitivity study has been performed for the involute spiral configuration. Due to the full size simulation, meshes contain relatively large number of elements, which are 7 million, 11 million, 18 million and 24 million respectively. The results are given in the involute spiral configuration results section.

2.3.7 Internal side results

Straight configuration

In this section the following sequence of duct design cases, as illustrated in Figure 2.3.5, are analyzed.

- Case A: concept with inflow duct guide vane only;
- Case B: Case A with improved outflow duct 'L' turn design and increased inflow duct area;
- Case C: Case B with 'Splitter 1' included;

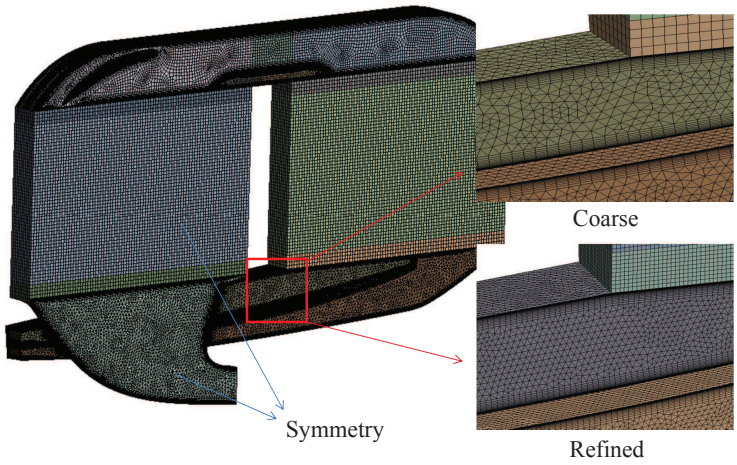

Figure 2.3.9: *Mesh for the internal side simulations of the straight tube configuration*

- Case D: Case C with crossover duct vane included;
- Case E: final design solution. Case D with 'Splitter 2' included.

A flow visualization of Case A is shown in Figure 2.3.11, from which it can be seen that the flow distribution pattern is greatly improved in the inflow tube stack. The separation in the inflow duct is also suppressed to a very low level, which gives a substantially reduced pressure loss. However, as the inflow passes the area where the inflow and outflow ducts intersect the available flow area has to be reduced. This leads to a local acceleration and then a relatively rapid deceleration over the leading edge area of the inflow guide vane. The associated adverse pressure gradient contributes to generate a vortex structure that extends over almost half of the chord length of the upper side of the inflow guide vane. This vortex is actually helping the flow distribution by suppressing the flow separation along the vane, but it contributes to a locally increased pressure loss. The net pressure loss for the inflow duct is however reduced as is seen in Table 2.3.2. Still, an increased area in the inflow outflow intersection region was believed to be effective in order to reduce the pressure loss in the inflow duct. As part of Case B, this was achieved by increasing the inflow duct height as illustrated in Figure 2.3.12.

With the improved L turn design of case B, see Figure 2.3.12 , it can be seen that the flow distribution of the outflow tube stack has been improved, but additional modifications are still needed to optimize the flow in the L turn and to improve the flow distribution of the outflow tube stack. The increased inflow duct area makes the flow distribution in the inflow tube stack worse. Although the vortex is now eliminated the flow starts to separate from the upper side of the vane. Still, the contribution of the increased inflow duct area leads to a remarkable improvement in the inflow duct pressure loss.

In the crossover duct a separation can be observed from the streamline plot in the top of Figure 2.3.13 as indicated by the encircled region. To reduce the pressure loss associated with this separation, a splitter ('Splitter 1') and a crossover duct vane are introduced. With only the 'Splitter 1' (Case C), the separation caused by the side wall boundary layer growth is suppressed, but a large separation from the upper wall is observed, see Case C of Figure 2.3.13. The addition of the cross over duct guide vane (Case D) largely eliminates the separation in the crossover duct as shown in the bottom of Figure 2.3.13. Although the separation is suppressed the use of crossover duct vane also increases the wetted area and hence there is no further reduction in pressure loss when both are applied, as seen from Table 2.3.2. However, a slight improvement in pressure loss in the tube stacks is observed. In total the introduction of 'Splitter 1' and the crossover duct vane reduces the pressure total loss of the intercooler and some pressure loss is re-distributed to the intercooler tube stacks. This re-distribution is believed to be beneficial since it may contribute to increasing the heat transfer capability of the intercooler. Furthermore, by comparing the total pressure loss incurred in the inflow duct, it can be seen that the introduction of the 'Splitter 1' reduces the pressure loss from 1.96% to 1.73% due to the re-distribution of the flow in the tubes stacks.

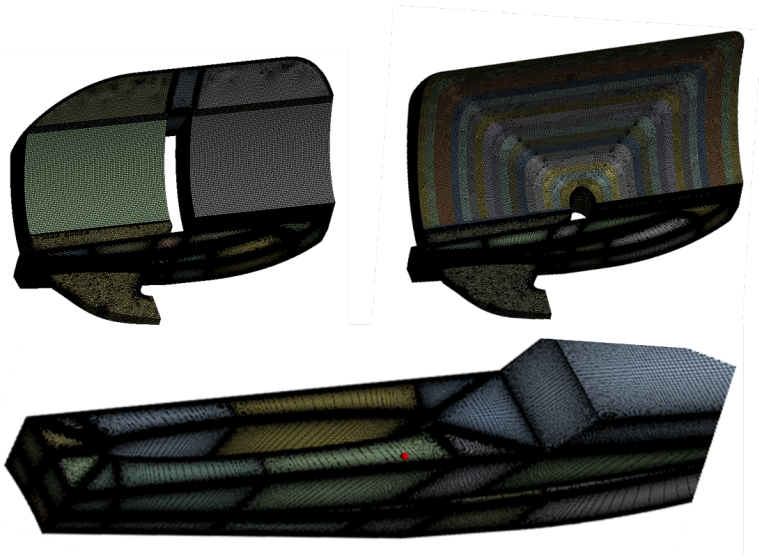

Figure 2.3.10: *Meshes for involute spiral (upper left) and U-bent (upper right) configurations, inflow duct mesh detail (lower).*

	Original	Case A	Case B	Case C	Case D	Case E
Inflow duct	3.36%	2.95%	1.96%	1.73%	1.73%	1.73%
Outflow duct	1.02%	1.08%	0.68%	0.69%	0.69%	0.70%
Crossover duct	0.24%	0.29%	0.27%	0.19%	0.19%	0.19%
Tube stacks (Porous media)	2.91%	2.78%	2.30%	2.38%	2.36%	2.32%
Net pressure loss	7.53%	7.10%	5.21%	4.99%	4.97%	4.94%

Table 2.3.2: Summary of internal side pressure loss distributions

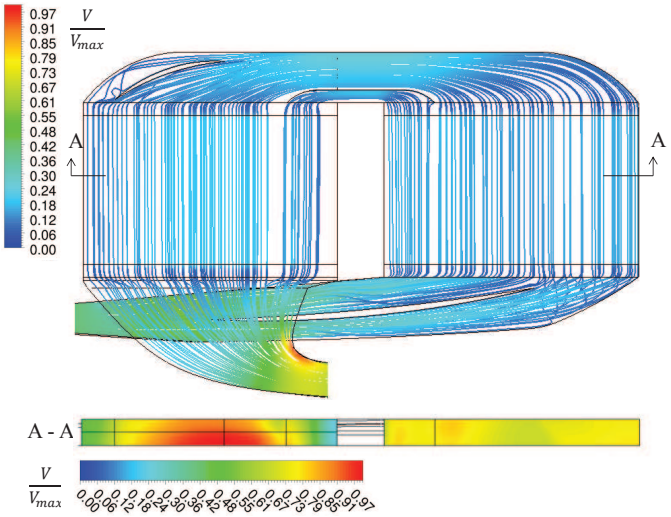

Figure 2.3.14: *Streamline plot of the internal side of the intercooler and velocity contour of the cross-section of the porous domain, case E*

The 'Splitter 1' and crossover duct vane did not contribute to improving the tube stack flow distribution. Actually, apart from the flow mal-distribution related to the corner separation of the crossover duct, the flow distribution in the intercooler tube stacks has degraded. From the A-A cross section velocity contours presented

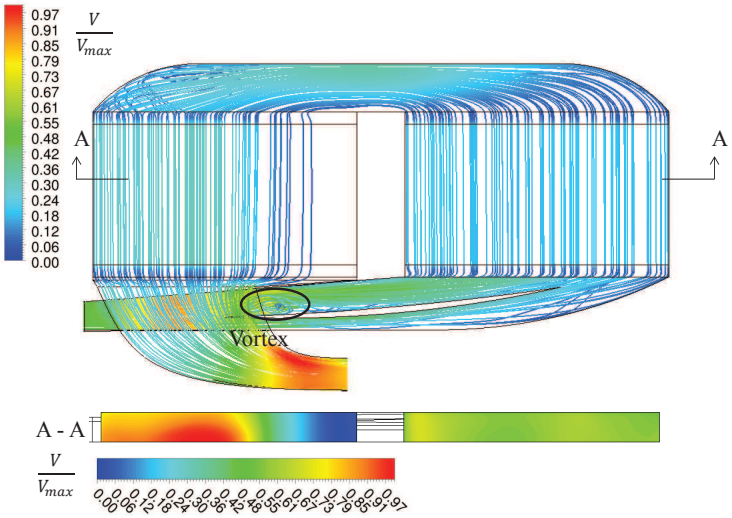

Figure 2.3.11: *Streamline plot of the internal side of the intercooler and velocity contour of the cross-section of the porous domain, case A*

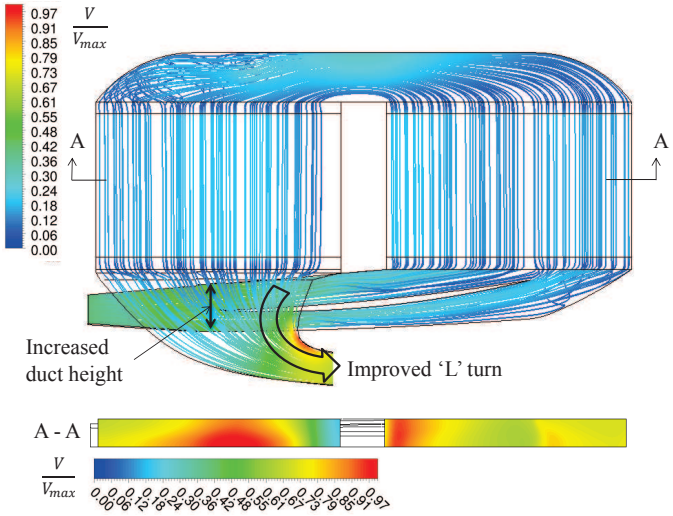

Figure 2.3.12: *Streamline plot of the internal side of the intercooler and velocity contour of the cross-section of the porous domain, case B*

in Figure 2.3.13, it can be seen that there are still some regions with flow mal-distribution. The final design modification studied in this paper, through the inclusion of 'Splitter 2' (case E), was intended to balance the flow by creating a channel directly connecting the rich flow part of inflow tube stack with the poor flow part of outflow tube stack. The result is shown in Figure 2.3.14 below, which shows a substantial improvement in the inflow tube stack flow distribution. The net pressure loss drops slightly as indicated in Table 2.3.2. In summary, the successive improvement of the original configuration leading up to the definition of Case E has resulted in a relatively well distributed intercooler flow pattern as seen from Figure 2.3.14.

Involute spiral configuration

For the design of the involute spiral configuration connecting ducts, the inflow guide vane and the outflow 'L' turn are also adopted. From the streamline plot, see Figure 2.3.15, it can be seen that the flow distribution is relatively good and no large separations occur in the ducts. The reasons for this good flow distribution, is partly due to the inflow duct guide vane and the outflow duct 'L' turn. Moreover, because the tubes are bent, the crossover duct is also designed to be bent following the same involute spiral line, which can be seen from Figure 2.1.2. This

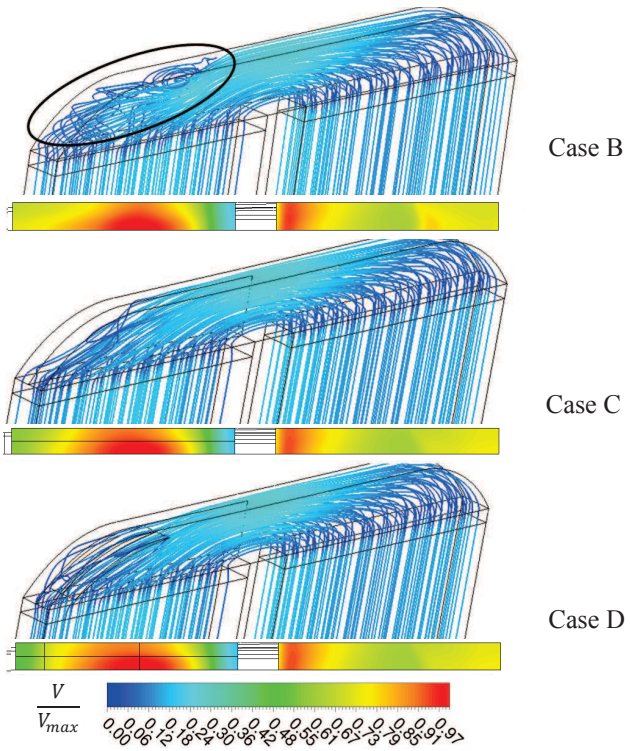

Figure 2.3.13: *Streamline plot of the crossover duct and velocity contour of the cross-section of the porous domain with corresponding cases B, C and D*

condition gives the flow a swirl motion in the crossover duct, which helps the flow resist the boundary growth and separation. Hence, no vane or splitter is needed in the crossover duct.

A mesh sensitivity study has been performed, with a 7 million, an 11 million, an 18 million and a 24 million elements mesh respectively for the involute spiral concept full size simulation. As illustrated in Figure 2.3.16, the velocity contours of the cross-sections of the porous media (tube stacks) are chosen to show the results. Generally, the results for all the cases show good consistence except a minor variation in the inflow porous media (right hand side). The variation in the inflow porous media is partly due to the unstable flow in the inflow duct and because a steady Reynolds Average Navier-Stokes (RANS) simulation is not able to capture the flow features. To fully converge this case, it is believed that an unsteady RANS solution would have to be established. The largest deviation between the mesh cases is 5% for total pressure loss. The case with 7 million elements is selected to build the connecting ducts performance correlations because of its lowest computation load and that the difference between the 7 million case and the 28 million case is modest.

U-bent configuration design

For the U-bent configuration, the same connecting ducts as for the involute spiral configuration are used, apart from the removal of the crossover duct. In the internal side simulations of the U-bent configuration, the tubes are modelled by a number of porous media blocks as shown in Figure 2.1.3 and Figure 2.3.10. Each porous media block represents one U-bent tube with the same length and pressure loss. A problem with this configuration that can be observed directly from Figure 2.3.17 is that the lengths of the tubes are varying considerably; a significant variation in the flow distribution can be seen from the velocity plot of the cross-section of the porous media blocks.

In order to balance the flow distribution, one solution is to vary the diameters of different tubes. Applying

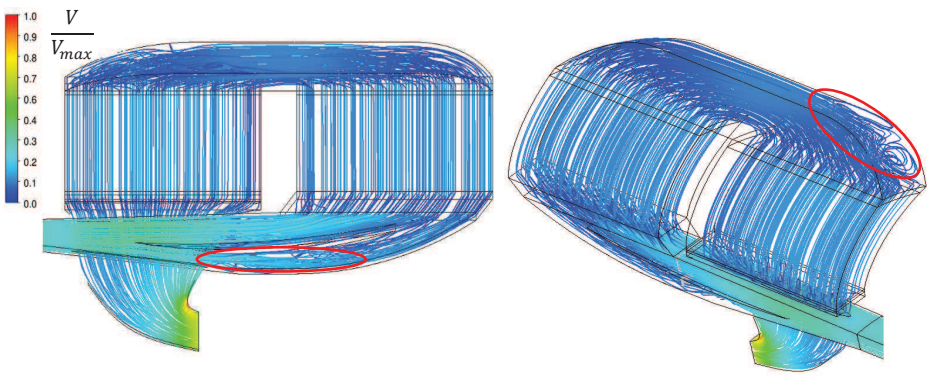

Figure 2.3.15: *Streamline plot of the internal side of the intercooler showing normal and backward view, for the involute spiral tube configuration*

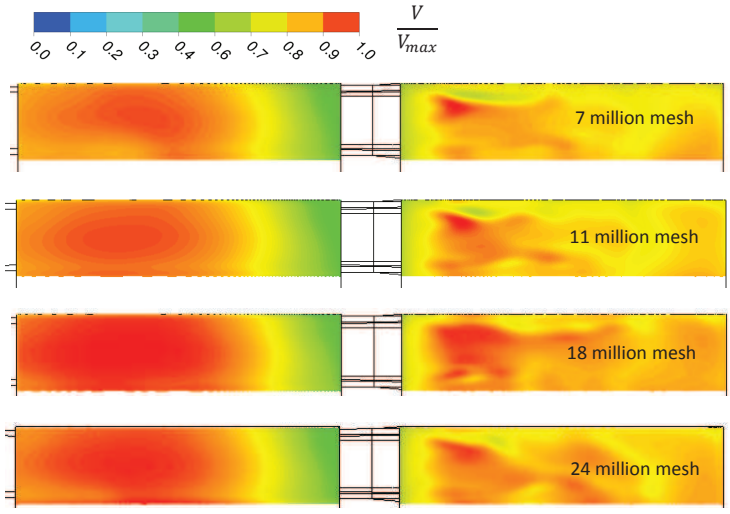

Figure 2.3.16: *Mesh sensitivity study for the involute spiral configuration, (a) 7 million, (b) 11 million, (c) 18 million and (d) 24 million; flow velocity contours of the cross-section of the porous media (tube stacks)*

the similar relation between the tube diameter and pressure loss for a circular pipe, the pressure loss and loss coefficient are increasing with a decreasing tube diameter. Hence, by using a smaller diameter on the shorter tubes, the increasing pressure loss can compensate the pressure loss difference resulting from different lengths. In addition, decreasing the tube diameter increases not only the pressure loss, but also the heat transfer. Figure 2.3.18 shows the result of an extreme case, the tube diameter, which is simulated by the corresponding loss coefficient, is varying for every two tube columns.

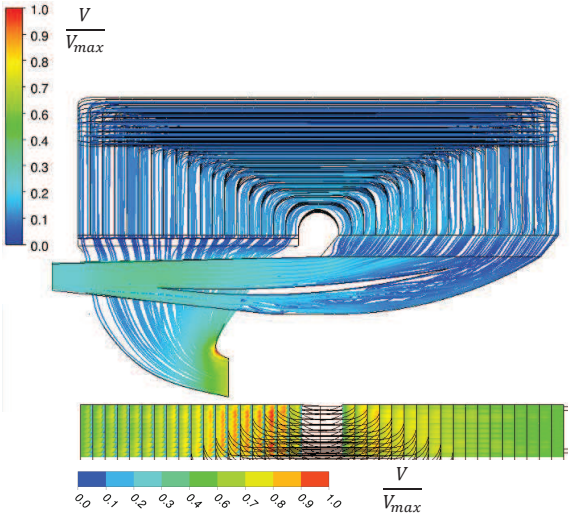

Figure 2.3.17: *Streamline plot of the internal side of the intercooler and velocity contour of the cross- section of porous domain, U-bent configuration*

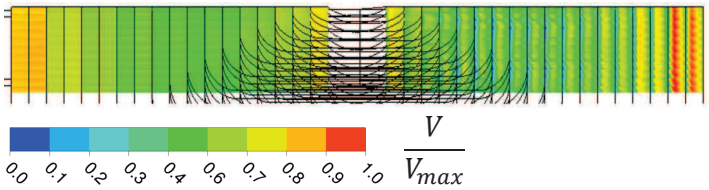

Figure 2.3.18: *Velocity contour of the cross-section of the porous domain, U-bent configuration with varying diameter tubes*

3 Intercooled geared engine performance

The selection of architecture for the intercooled engine is generally based on two considerations. Firstly, a three shaft or a geared concept is more easy to use to when a relatively high intercooler entry pressure is required. Secondly, although a high HPC exit temperature arising from a high OPR can be avoided by intercooling, there is still a risk of an HPC efficiency drop due to a small blade height and a large hub/tip ratio. A geared turbofan variant, is proposed to mitigate this effect [34, 35]. For a geared turbofan, the low pressure turbine (LPT) has a higher rotational speed than in the conventional turbofan, for which the rotational speed of the low pressure shaft is limited by the fan tip speed. The increased shaft speed allows for a smaller shaft diameter that makes it possible to integrate the HPC at a lower radius. This increases last stage blade height. Furthermore, for the LPT, an increased rotational speed also gives a lower blade loading, higher efficiency and allows the use of fewer stages. Hence, the bypass ratio can be ultra-high without an excessive number of LPT stages.

3.1 Engine modelling parameters

In order to show the benefit that the intercooler could bring, an advanced non-intercooled geared engine is modelled as the reference engine for comparison. The advanced non-intercooled geared engine is optimized by varying the bypass ratio, fan, IPC and HPC pressure ratio. The OPR is limited due to the turbine blade and disc cooling temperature, as manifested by a maximum compressor exit temperature of 950 K. The engine take-off net thrust is set to be 65625 lbf which is considered suitable for the twin engine aircraft model used for this study. Design point data and constraints common to the geared and the intercooled geared engine are summarized in Table 3.1.1 below. The efficiencies in the table are polytropic. T_{blade} is the allowed maximum blade temperature. A hot day take-off condition is used to evaluate the engine at the start of the mission analysis. The cooling flow is then calculated based on the model established in [11].

Parameter	Value
$T_{HPC,exit}$	$< 950K$
$T_{Combustor,exit}$	$< 1900K$
T_{blade}	$< 1210K$
η_{fan}	93.5%
η_{IPC}	92.2%
η_{HPC}	92.5%
η_{HPT}	90.7%
η_{IPT}	91.4%
η_{LPT}	93.25%

Table 3.1.1: Design point performance parameters (take-off)

The data presented in Table 3.1.1 are based on estimates on performance levels achievable for an engine entering into service year 2020+. The optimization procedure establishes an engine that provides minimum fuel burn for a fixed mission and fixed aircraft. The mission length is 6800 km. Initial cruise altitude is 35000 ft. and final cruise altitude is 39000 ft. A trade factor is established to estimate the full fuel burn saving potential for a scalable aircraft.

3.2 Intercooler parameters and installation

After having the performance characteristics of the two-pass cross flow intercooler, the geometric parameters of the intercooler and the intercooler installation space should be taken into account. Proper constraints need to be set to avoid an intercooler with an extreme size.

The tube diameter is given by the major axis length of the tube, since the aspect ratio is fixed in this thesis. As the size of the tube is decreasing, the total perimeter length of the tubes increases for a given cross sectional

area which leads to an increase of the wetted area.

The tube length, which is set by the radial position of the diffuser and the inner diameter of the internal bypass duct, is limited by the need to minimize the external bypass flow Mach number, the nacelle maximum diameter and the internal bypass diffusion loss. However, an increased tube length gives larger frontal area which in turn gives a lower flow Mach number through the intercooler and hence a lower intercooler external side pressure loss as well as more heat transfer area.

Basically, the total heat transfer area is determined by the single tube size and the number of tubes. The number of tubes is equal to the number of tube rows (circumferential direction) multiplied by the number of tube columns (axial direction). The distribution between the number of rows and the number of columns plays an important role in the intercooler performance. Generally, with a given single tube size and heat transfer area, fewer columns are desirable for decreasing the external side pressure loss. A high radius installation of the intercooler gives more rows and fewer columns but also increases the nacelle diameter.

The estimation of the number of tube rows and columns in the two intercooler stacks requires an iterative design process. Since the mass flow, temperature and pressure at the intercooler internal side inflow are given from engine boundary conditions, the assumption of a Mach number on the internal side of the tubes will lead to an estimate of the total internal flow area. For a given tube diameter the required number of tubes can then be calculated. Having defined the location of the intermediate and high pressure compressor interfaces as well as the available radial space for installing the intercooler, the total number of tube rows around the circumference can be estimated. This then allows the calculation of the number of tube columns.

In order to reduce the number of design parameters, the flow Mach number inside the tubes can be fixed to a preferred value. This was done after a number of preliminary optimization studies revealed that the optimizer always produced the lowest internal tube Mach number allowed in the optimization. Low values may lead to designs that could not be fitted within the available space constraints. Attempts to increase the external nacelle diameter to accommodate a larger intercooler resulted in an increase in mission fuel burn. The nacelle line moves with the change in intercooler size, in order to keep the external bypass flow, as illustrated in Figure 1.3.1, Mach number lower than 0.6.

Furthermore, the additional weight and nacelle diameter caused by the intercooler has been considered. Titanium is assumed to be used as the intercooler material. The tube thickness is calculated based on the pressure difference between the inner and outer side of the tube. A minimum tube thickness is assumed to be 0.2 mm.

3.3 Coolant mass flow control

Controlling the coolant flow may give a benefit by allowing the intercooler to operate at the most suitable condition depending on the flight phase. For instance, at the cruise phase, reducing the coolant mass flow reduces intercooler external Mach numbers and related pressure losses, both over the intercooler and in the upstream intercooler diffuser. The reducing of the coolant mass flow also decreases transferred heat, which leads to an increased combustor inlet temperature and a reduced fuel flow need. Two options are available to achieve this control as mentioned in the introduction chapter. A more detailed discussion for the variable mixer and the auxiliary variable nozzle is given here.

3.3.1 Variable mixer

A schematic drawing of the variable mixer is illustrated here in Figure 3.3.1. The external bypass flow and the internal bypass flow, which the latter is the coolant flow downstream of the intercooler, are mixed together before the nozzle exit. The total nozzle area is fixed, while the area ratio between the external and internal bypass flow before the mixing can be varied to control the intercooler coolant mass flow, through a variable geometry as indicated by the dash line.

However, this geometry is not adopted here, mainly due to the problem induced by the pressure match at the mixing plane. As it will be seen later in the results, the intercooler external pressure loss at take-off is around 15%. With this high pressure loss, a very high Mach number is required for the external bypass flow to match the low pressure of the internal bypass flow stream, which is not applicable. In addition, the engine performance is

quite sensitive to the mixing loss of this variable mixer. An ideal mixing assumption will then be too optimistic for the performance evaluation.

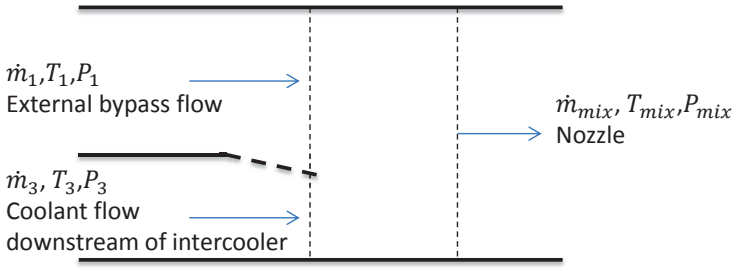

Figure 3.3.1: *Variable mixer flow streams*

3.3.2 Auxiliary variable nozzle

The advantage of the auxiliary variable nozzle, compare to the variable mixer, is the freedom of control. As shown in Figure 3.3.2, the auxiliary nozzle is able to control the coolant mass flow by adjusting the nozzle area independently and hence, this geometry was used in the performance evaluation presented later.

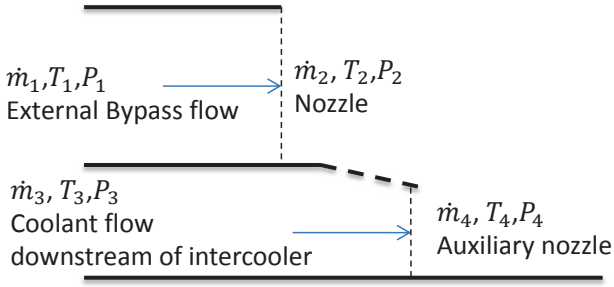

Figure 3.3.2: *Auxiliary variable nozzle flow streams*

3.4 Performance evaluation

After a number of preliminary optimization studies the following intercooler parameters were used as shown in Table 3.4.1.

Ellipse major axis length	30.7 mm
Number of tube columns per stack	20
Number of tube rows per stack	11
Number of tube stacks	2×24 (two pass)
Tube arrangement	Case B, m=2, n=1
Mach number in tube (take-off)	0.07
Tube length	0.37 m
Intercooler height	0.43 m
Intercooler length	1.3 m
Intercooler weight	309 kg
Intercooler configuration	Involute spiral

Table 3.4.1: Two-pass cross flow tubular intercooler parameters for the optimized intercooled geared engine

The use of a separate variable exhaust nozzle can considerably reduce the irreversibilities associated with the coolant flow and limit the heat rejection from the core. However, the fan mass flow decreases when the auxiliary

nozzle area is decreasing. Hence, the specific thrust level is going up and this deteriorates the benefit through a decreased propulsive efficiency. As shown in Table 3.4.2, an optimal point can be found where the decreased propulsive efficiency starts to active.

Cruise phase	Nozzle 100%	Nozzle 60%	Nozzle 30%	Nozzle 10%
OPR	79	76	74	73
Fan mass flow (kg/s)	406	393	382	374
Core flow temperature drop (K)	-84	-75	-59	-31
Coolant flow pressure loss	-23.5%	-11.7%	-3.8%	-0.55%
Coolant mass flow (kg/s)	39.5	28.2	15.0	5.0
Cruise SFC (mg/Ns)	13.41	12.85	12.68	12.72
Cruise $\eta_{thermal}$	0.509	0.532	0.542	0.543
Cruise $\eta_{propulsive}$	0.809	0.809	0.805	0.801

Table 3.4.2: Coolant flow control results

Notice that this behavior is opposite to how the engine reacts to a variable mixer (for which the total exhaust nozzle area will not change). For this configuration a reduced area for the coolant flow passage will reduce the pressure loss over the intercooler surface and so is the heat transfer, giving a lower temperature and higher stagnation pressure in the flow. To keep the corrected flow in the nozzle constant the mass flow must increase in the external bypass (assuming that the nozzle is choked in top-of-climb and cruise). Hence, a higher propulsive efficiency can be expected for the variable mixer.

	Advanced non-IC geared	Intercooled geared
OPR	61	81
TOC OPR	76	101
Cruise OPR	58	75
BPR	15.42	16.74
FPR	1.40	1.44
IPC PR	4.91	4.55
HPC PR	7.72	13.78
HPC last blade height (mm)	19.4	13.6
HPC last blade hub/tip ratio	0.91	0.92
HPC exit temperature at take-off (K)	941.9	888.4
HPT cooling bleed ratio	0.19	0.14
Take-off SFC (mg/Ns)	6.28	6.17
TOC SFC (mg/Ns)	13.07	12.93
Cruise SFC (mg/Ns)	13.10	12.68
Cruise $\eta_{thermal}$	0.514	0.541
Cruise $\eta_{propulsive}$	0.823	0.806
Engine weight (kg)	7005	6705
Nacelle diameter (mg/Ns)	3.47	3.49
Mission fuel burn (kg)	base	-935 (-3.2%)

Table 3.4.3: Optimal engine configurations

For the advanced non-intercooled geared turbofan engine, the optimal OPR (take-off) is found to be 61, whereas for the intercooled engine an OPR of 81 is obtained. For the intercooled geared turbofan, a further reduction in mission fuel burn can be achieved for an even higher OPR. However, the minimum compressor blade height constraint of the HPC then becomes active.

As a result, a high thermal efficiency is observed as seen in Table 3.4.3 and a cruise SFC benefit of 3.2% is obtained for the intercooled engine comparing to the non-intercooled geared engine. For the fixed aircraft mission this integrated to a 3.2% fuel burn benefit. The largest benefit is gained from the low coolant mass flow at

cruise condition, as established by the use of the auxiliary nozzle. In addition, the intercooler also contributes to a reduced engine core size through an increase in the specific power of the core, resulting in an estimated 300 kg weight reduction. The nacelle diameter is only slightly changed for the intercooled engine contributing only marginally to the fuel burn change.

4 Conclusions

In general the two-pass cross flow intercooler has been seen to give a relatively small internal pressure loss. A relatively high external pressure loss has been observed, but this could be limited quite effectively in cruise by the use of the variable exhaust nozzle. The transferred heat with this intercooler concept is relatively modest. It is however sufficient to enable the higher OPR which is restricted by the compressor exit temperatures for the advanced non-intercooled geared engine. An OPR of 75 was achieved in cruise compared to an OPR of 55 for the advanced non-intercooled engine. The intercooled engine OPR is actually higher if the auxiliary nozzle area is kept at its design value, but there is a net gain in fuel burn reduction from reducing its area. The intercooling also allowed for a somewhat smaller core size giving a considerable benefit in reduced weight.

A further increase in OPR for the intercooled engine will suffer a rapid efficiency drop of the HPC due to very short blades. As seen from Table 3.4.3, the intercooled engine HPC take-off exit temperature is quite far away from the limit, around 60 K lower. Even without any further utilization, a benefit is still obtained from the reduced compressor exit temperature through a reduced cooling flow need. Potentially, the reduced compressor exit temperature could also be used to reduce NO_x emissions.

The optimal amount of intercooling will ultimately depend on the intercooler performance, but the experience drawn from this work is that enabling the OPR and possibly reducing the compressor exit temperature somewhat further maximizes efficiency. With a lower HPC delivery temperature, the combustor has a larger temperature rise and the core mass flow can be reduced (at a fixed turbine entry temperature), increasing bypass ratio (at a fixed fan diameter), thus reducing the size and weight of the core and of the intercooler ducting and possibly also of the intercooler itself. While designing for a higher HPC exit temperature and less intercooling will provide net benefits stemming from reduced pressure losses and reduced heat transfer at cruise condition, which will both contribute to improve the engine SFC. Also, an intercooler with a lower design effectiveness would directly reduce its weight and size, hence the weight of the engine and the nacelle diameter. Therefore, determining an optimal intercooled engine requires multidisciplinary understanding and a number of sufficiently accurate correlations.

Bibliography

[1] AIRBUS S.A.S. Future Journeys 2013-2032, Global Market Forecast.

[2] M. Daly and B. Gunston. *Jane's Aero-Engines, Issue Twenty-seven.* IHS Jane's, ISBN 1748-2534, 2010.

[3] J. Jane. Fully Enhanced Gas Turbine For Surface Ships. *ASME96-GT-527*, 1996.

[4] M. J. Reale. New High Efficiency Simple Cycle Gas Turbine - GE's LMS100. Technical report, GE Energy, 2004.

[5] C. McDonald, A. Massardo, C. Rodgers, and A. Stone. Recuperated Gas Turbine Aeroengines, Part I: Early Development Activites. *Aircraft Engineering and Aerospace Technology: An International Journal*, 80(2):139–157, 2008.

[6] C. McDonald, A. Massardo, C. Rodgers, and A. Stone. Recuperated Gas Turbine Aeroengines, Part II: Engine Design Studies Following Early Development Testing. *Aircraft Engineering and Aerospace Technology: An International Journal*, 80(3):280–294, 2008.

[7] C. McDonald, A. Massardo, C. Rodgers, and A. Stone. Recuperated Gas Turbine Aeroengines, Part III: Engine Concepts for Reduced Emissions, Lower Fuel Consumption, and Noise Abatement. *Aircraft Engineering and Aerospace Technology: An International Journal*, 80(3):408–426, 2008.

[8] K. Kyprianidis, T. Grönstedt, S. O. T. Ogaji, P. Pilidis, and R Singh. Assessment of Future Aero-Engine Designs with Intercooled and Intercooled Recuperated Cores. *Journal of Engineering for Gas Turbines and Power*, 133(11), Jan. 2011.

[9] G. Wilfert, J. Sieber, A. Rolt, N. Baker, A. Touyeras, and S Colantouni. New Enviromentally Friendly Aero Engine Core Concepts. *The 18th International Symposium on Air Breathing Engines, Beijing, China, ISABE-2007-1120*, Sep. 2007.

[10] A. Lundbladh and A Sjunnesson. Heat Exchanger Weight and Efficiency Impact on Jet Engine Transport Applications. *The 16th International Symposium on Air Breathing Engines, Cleveland, Ohio, ISABE-2003-1122*, Sep. 2003.

[11] R. C. Wilcock, J. B. Young, and J. H. Horlock. The Effect of Turbine Blade Cooling on the Cycle Efficiency of Gas Turbine Power Cycles. *Journal of Engineering for Gas Turbines and Power*, 127, Jan 2005.

[12] W. M. Kays and A. L. London. *Compact Heat Exchanger, 2nd ed.* McGraw-Hill, ISBN 07-033391-2, 1964.

[13] L. Xu. *Analysis and Evaluation of Innovative Aero Engine Core Concepts.* PhD Thesis, Chalmers University of Technology, Gothernburg, Sweden, 2011.

[14] P. Naphon and S. Wongwises. A review of flow and heat transfer characteristics in curved tubes. *Journal of Renewable and Sustainable Energy Reviews*, 10(5):463–490, 2006.

[15] G.H. Keulegan and K.H. Beij. Pressure losses for fluid flow in curved pipes. *Journal of Research of the National Bureau of Standards*, 18:89–114, 1937.

[16] W. A. Khan, J. R. Culham, and M. M. Yovanovich. Fluid Flow Around and Heat Transfer from Elliptical Cylinders. *Journal of Thermophysics and Heat Transfer*, 19(2), April-June 2005.

[17] H. Grieb and W. Schlosser. Shaped Tube with Elliptical Cross-section for Tubular Heat Exchangers and a Method for Their Manufacture. *United States Patent*, (4766953), August 1988.

[18] ANSYS Inc. Innovative Turbulence Modeling: SST Model in ANSYS CFX. Technical report, ANSYS Inc., Canonsburg, PA, 2006.

[19] F. Menter, J.C. Ferreira, T. Esch, and B. Konno. The SST Turbulence Model with Improved Wall Treatment for Heat Transfer Predictions in Gas Turbines. *Proceeding of the International Gas Turbine Congress, Tokyo*, Nov. 2003.

[20] Q. Xiao and H.M. Tsai. Numerical investigation of Supersonic Nozzle Flow Separation. *AIAA journal*, 45:532–541, 2007.

[21] T. Grönstedt. *Development of Methods for Analysis and Optimization of Complex Jet Engine Systems.* PhD Thesis, Chalmers University of Technology, Gothernburg, Sweden, 2000.

[22] A. D. Walker, G. S. Regunath, J. F. Carrotte, and P. A. Denman. Intercooled Aero-Gas-Turbine Duct Aerodynamics: Core Air Delivery Ducts. *Journal of Propulsion and Power*, 28(6), Nov.-Dec. 2012.

[23] A. D. Walker, J. F. Carrotte, and A. M. Rolt. Duct Aerodynamics for Intercooled Aero Gas Turbines: Constraints, Concepts and Design Methodology. *Proceedings of ASME Turbo Expo 2009: Power for Land, Sea and Air, GT2009-59612*, June 8-12 2009.

[24] L. Xu and T Grönstedt. Design and Analysis of an Intercooled Turbofan Engine. *Journal of Engineering for Gas Turbines and Power*, 132, Nov. 2009.

[25] K. Kritikos, C. Albanakis, D. Missirlis, Z. Vlahostergios, A. Goulas, and P. Storm. Investigation of the Thermal Efficiency of a Staggered Elliptic-tube Heat Exchanger for Aeroengine Applications. *Applied Thermal Engineering*, 30:134–142, 2010.

[26] D. Missirlis, S. Donnerhack, O. Seite, C. Albanakis, A. Sideridis, K. Yakinthos, and A. Goulas. Numerical Development of a Heat Transfer and Pressure Drop Porosity Model for a Heat Exchanger for Aeroengine Applications. *Applied Thermal Engineering*, 30:1341–1350, 2010.

[27] D. Missirlis, K. Yakinthos, A. Palikaras, K. Katheder, and A. Goulas. Experimental and Numerical Investigation of the Flow Field through a Heat Exchanger for Aeroengine Applications. *Int. J.Heat and Fluid Flow*, 26:440–458, 2005.

[28] ANSYS Ltd. *Ansys CFX Help.* ANSYS Ltd., release 12.0 edition, 2010.

[29] S. E. Haaland. Simple and explicit formulas for the friction factor in turbulent pipe flow. *J. Fluids Eng.*, 105(1):89–90, 1983.

[30] H. Grieb. *Projektierung von Turboflugtriebwerken.* Birkhäuser, ISBN 3-7643-6023-2, 2004.

[31] F.M. White. *Fluid Mechanics, 6th ed.* McGraw-Hill, 2008.

[32] C.L. Ford, J.F. Carrotte, and A.D. Walker. The Application of Porous Media to Simulate the Upstream Effects of Gas Turbine Injector Swirl Vanes. *Computers and Fluids*, 77, 2013.

[33] S.L. Dixon and C.A. Hall. *Fluid Mechanics and Thermodynamics of Turbomachinery, 6th ed.* Elsevier, 2010.

[34] X. Zhao, T. Grönstedt, and K. Kyprianidis. Assessment of The Performance Potential for a Two-pass Cross Flow Intercooler for Aero Engine Applications. *The 21th ISABE conference, September 9-13, Busan, South Korea*, 2013.

[35] K. Kyprianidis, A. Rolt, and T. Grönstedt. Multidisciplinary Analysis of a Geared Fan Intercooled Core Aero-Engine. *Journal of Engineering for Gas Turbines and Power*, 136(1), Oct. 2013.

Paper A

Zhao, X. and Grönstedt, T., **Conceptual Design of a Two-Pass Cross Flow Aero-Engine Intercooler**. Submitted to Journal of Engineering for Gas Turbine and Power.

Conceptual Design of a Two-Pass Cross Flow Aero-Engine Intercooler

Xin Zhao
Ph.D Student
Chalmers University of Technology
SE-412 96 Göteborg, Sweden
Email: xin.zhao@chalmers.se

Tomas Grönstedt
Professor
Chalmers University of Technology
SE-412 96 Göteborg, Sweden
Email: tomas.gronstedt@chalmers.se

ABSTRACT

Establishing an optimal intercooled aero engine constitutes a coupled problem where the conceptual design of the intercooler and the engine has to be considered simultaneously. The heat transfer and pressure loss characteristics will depend on the choice of the intercooler architecture. Hence, to be able to optimize the performance of an intercooled aero engine, the performance characteristics of a given intercooler architecture has to be known in the parameter range anticipated for the aero engine optimization. Here, the conceptual design of a tubular two-pass cross flow intercooler architecture intended for a turbofan aero engine application is presented. The internal flow is simulated applying a porous media model for the intercooler tubes, whereas the connecting ducts are analysed with three-dimensional simulations allowing the assessment of a number of design solutions. The external flow is treated with two-dimensional simulations investigating the external pressure loss and heat transfer characteristics of the two elliptical tube stacks. The intercooler performance is then generalized by developing a reduced order correlation covering a parameter range anticipated for a turbofan conceptual design optimization. In addition to providing heat transfer and pressure loss characteristics, the correlations are set up to allow intercooler installation space constraints to be taken into account.

Nomenclature

A_c Minimum flow cross section area of the computational domain $[m^2]$
A_f Intercooler frontal area of the computational domain $[m^2]$
A_w Heat transfer wall area of the computational domain $[m^2]$
a Major axis length of the ellipse $[m]$
b Minor axis length of the ellipse $[m]$
D Hydraulic diameter of single elliptical tube $[m]$
D_h Hydraulic diameter of a tube stack computational domain $[m]$
d_a Axial spacing between tube columns $[m]$
d_b Transversal spacing between tube rows $[m]$
f Friction factor
h Heat transfer coefficient $[J/(m^2 \cdot s \cdot K)]$
j Colburn j factor
k_{tube} Tube internal flow loss coefficient
k' Darcy pressure loss coefficient for porous media model
L Total flow length of the intercooler $[m]$
$\dot{m}$ Mass flow rate $[kg/m^3]$
V Flow Velocity $[m/s]$
Nu Nusselt number
Pr Prandtl number
Re Reynolds number
St Stanton number
Δp Pressure drop $[Pa]$

ρ Density $[kg/m^3]$
μ Dynamic Viscosity $[kg/(m \cdot s)]$
κ Thermal conductivity of air $[J/(m \cdot s \cdot K)]$

1 Introduction

Intercooled aero engines may provide a number of benefits such as reduced specific fuel consumption (SFC) through increased overall pressure ratios (OPR), a reduced high pressure turbine cooling air requirement through reduced cooling air temperatures and reduced NO_x emissions through reduced combustor flame temperatures [1–6]. In conventional engines the OPR is limited by compressor exit temperature constraints set primarily by high pressure turbine disc and blade cooling requirements. Thus, a decreased compressor exit temperature provided through intercooling allows increased OPR which enables increased thermal efficiency and reduced SFC. These potential benefits can be realized if the additional pressure losses caused by the flow through the intercooler can be kept at a sufficiently low level. For aero engine applications it is particularly important to achieve a compact intercooler design. The engine installed SFC is directly influenced by increased nacelle drag in terms of nacelle diameter and length. If the installation becomes bulky there will be an increase in the nacelle diameter, hence an increase in the nacelle drag. Increased volume may also lead to difficulties diffusing the intercooler inflow, add to shaft lengths and cause vibration problems. Additionally, the added intercooler weight penalty must be compensated for by the engine performance improvement that intercooling introduces.

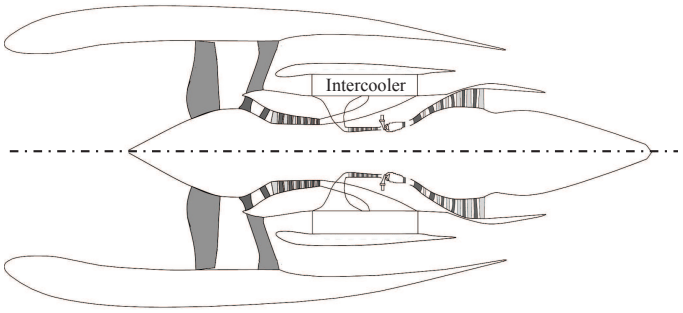

Fig. 1: Intercooled engine arrangement with two-pass cross flow configuration [7].

An intercooler may be integrated anywhere in the compressing process downstream of the fan, but positioning it too early will reduce the performance through pressure loss and weight penalties. Engine architectures suitable for integration would be three-shaft and geared concepts which can be designed with a relatively high pressure ratio on the upstream compressor. In this work, the intercooler is configured between the intermediate pressure compressor (IPC) and the high pressure compressor (HPC) of a three-shaft turbofan engine as shown in Figure 1.

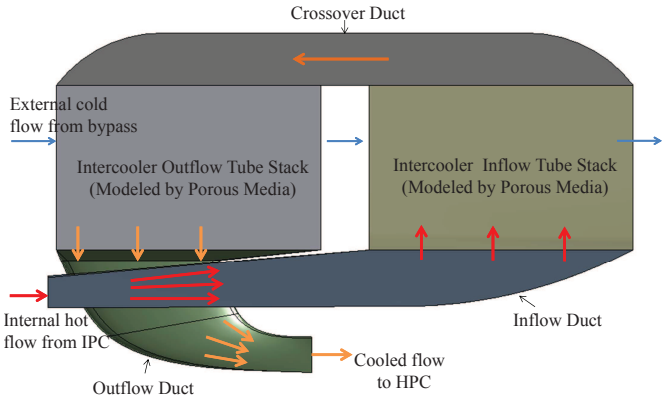

Fig. 2: Layout of the two-pass cross flow intercooler concept

Walker et al. [8, 9] have, in their experimental and computational work on developing a ducting system for a single pass corrugated intercooler, summarized what the desired internal ducting system must provide to work satisfactorily; a low aerodynamic loss combined with a uniform flow distribution through the heat transfer units in order to achieve a high cooling effectiveness. On the internal side of the intercooler studied herein, the connecting ducts incur a considerable part of the total pressure loss while their contribution to heat transfer is negligible. Previous studies reported for this two-pass

cross flow configuration [7, 10] applied correlation based methods for assessing the performance of the connecting ducts. These correlations were based on simplified and general duct geometries which were not able to accurately evaluate the performance of the intercooler installation. For this reason, a three-dimensional CFD study with porous media modeled tubes stacks has been carried out to establish a more realistic assessment of the ducting system for the intercooler.

On the external side of the two-pass cross flow intercooler analyzed here, a parametric study of the staggered tubes configuration has been conducted. The pressure loss incurred over the tubes is necessary to generate the heat transfer and a trade-off between heat transfer and pressure loss must be established in order to determine the optimal intercooler design. Going to higher levels of pressure loss has the drawback that fluid acceleration due to reduced stagnation pressure and heat addition tend to drive the loss levels up quickly, while lower pressure loss levels require excessive volume or tend to make the heat transfer insufficient.

The ultimate selection of configuration is a matter of research and it is the intention to provide some additional information through this work. The contribution presented in this paper is viewed to relate to two efforts. Firstly, the intercooler configuration has undergone several design iterations, including systematic geometry parameter variation and analysis as well as considering fundamental design changes such as including inlet guide vanes in the inflow duct of the intercooler. Secondly, heat transfer and loss characteristics have been correlated to a parameter range covering the expected installed conditions experienced in take-off, top-of-climb and mid-cruise allowing independent engine performance assessments of this intercooler concept. To the knowledge of the authors no set of correlations based on the conceptual design of an intercooler, targeting an aero engine application, is available in open literature.

2 Intercooler External Side Modelling

To explore the intercooler external pressure loss and heat transfer characteristics the inter-tube spacing was systematically varied. A schematic sketch of the problem configuration and an overview of the computational domain is shown in Figure 3. The range for the d_a and d_b parameters are given in Table 1.

As presented in [11], the heat transfer capability of elliptical cylinders increases rapidly from an aspect ratio around two up to an aspect ratio around eight after which there is only a limited improvement. Here an aspect ratio of 8.0 is selected for the tube ellipse, which gives almost twice the perimeter of the circle with the same area. This was done in order to increase the heat transfer area for a given internal cross sectional area, while having a good aerodynamical shape that reduces the risk for flow induced vibrations. Elliptic shaped tubes run the risk of deformation due to the pressure difference between the internal and the external side. However, it is believed that the suggested tube geometry can be produced in a way that it will maintain its shape during operation. A manufacturing process for this type of tube is described in [12].

The data given in Table 1 represents the boundary conditions used in the parametric study of the external side. The inlet flow Mach number is varied to establish correlations in the average flow field Reynolds number range $10,000 < Re < 120,000$. This covers a sufficient range to allow assessing the performance of an intercooled engine.

To resolve the boundary layers around the elliptical tubes, the meshes were generated to get $y^+ < 1.0$. A mesh independency study was performed to establish the final mesh settings to be used for all the cases. Three hybrid meshes which have maximum face size 0.4 *mm*, 0.3 *mm*, 0.2 *mm*, resulting in around 0.7 million, 1.0 million and 1.7 million elements respectively have been compared. The results show that the relative deviation in stagnation pressure between the 0.7 million and 1.0 million cases was around 2% and the difference between the 1.0 million 1.7 million was 0.6%. To achieve a reasonably accurate results without excessive computation time, the 1.7 million elements mesh was considered sufficient. The computations are performed using ANSYS CFX, which is a commercial CFD software. The shear stress transport (SST) turbulence model is adopted here, which has shown to give reasonably good predictions of separation and possible flow recirculation modelling [13, 14]. For the evaluation of the heat transfer and aerodynamic properties of the external side of the intercooler, the dimensionless heat transfer coefficient, the Colburn j factor, is introduced [15]:

$$j = St \cdot Pr^{2/3} = \frac{Nu}{Re \cdot Pr} \cdot Pr^{2/3} \tag{1}$$

The Nusselt number, the Reynolds number of the flow field and related hydraulic diameter are calculated from the expressions suggested by Kays and London [15]:

$$D_h = \frac{4A_cL}{A_w} \; ; \quad Nu = \frac{hD_h}{\kappa} \; ; \quad Re = \frac{(\dot{m}/A_c) \cdot D_h}{\mu} \tag{2}$$

where h is the local heat transfer coefficient; D_h is the hydraulic diameter of the flow field; k is the thermal conductivity of air; A_w is the surface area of the ellipses; A_c is the minimum flow cross sectional area and L is the total flow length of the

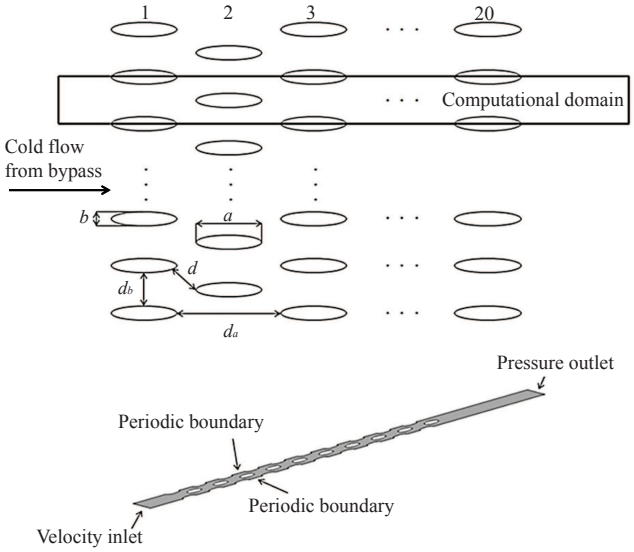

Fig. 3: Intercooler external side computational domain

Distance along the external side flow direction $d_a = n \cdot a$	$n = 0.75, 0.8786, 1$
Distance along the transversal direction $d_b = m \cdot b$	$m = 1, 2, 3$
Ellipse aspect ratio	$a/b = 8/1$
Temperature at the wall	556 K
Inlet flow Mach number	$0.05 - 0.2$
Inlet flow temperature	349 K
Outlet pressure	1 bar

Table 1: Intercooler external side parameter range and boundary conditions

intercooler. The friction factor f is defined through [15]:

$$\Delta p = \frac{(\dot{m}/A_c)^2}{2\rho_i}[f\frac{A_w}{A_c}\frac{\rho_i}{\rho_m} + (1+\sigma^2)(\frac{\rho_i}{\rho_o} - 1)] \tag{3}$$

where ρ_i and ρ_o are the fluid inlet and outlet density, ρ_m is the average of ρ_i and ρ_o, σ is the ratio between the minimum flow cross sectional area A_c and the intercooler frontal area A_f, and $\dot{m}$ is the mass flow at the inlet. In this equation the friction factor f represents an equivalent shear force per unit area in the flow direction composed of the true viscous shear forces as well as the pressure forces.

3 Intercooler Internal Side Modelling

3.1 Porous Media Modelling

The introduction of a porous media model for calculating properties of the internal side intercooler tube stacks allows realistic loss modelling when calibrated. The advantage is that the entire intercooler can be treated in a single three-dimensional simulation allowing interactions between the connection ducts and the intercooler tubes to be studied at an affordable computational effort. Missirlis et al. [16–18] have shown that, without the need for details of the flow in the tube stacks, porous media can sufficiently well describe the macroscopic behaviour of the heat exchanger. This is a quite valuable approach since the pressure losses in the intercooler tubes strongly influence the flow distribution in the connection tubes and conversely any flow mal-distribution will have a strong effect on the pressure loss distribution in the intercooler tubes.

The porous media simulations are based on the Darcy pressure drop law, set up with a directional pressure loss model.

The stream-wise directional loss is determined by the quadratic resistance coefficient k', see [19, 20], defined as:

$$\frac{\Delta p}{\Delta x} = -k'V|V| \tag{4}$$

where V is the true velocity of the flow assuming an even flow distribution, and Δp is the pressure loss along tube with length Δx. To keep the stream-wise direction as the unique flow direction, the transverse directional loss coefficient is increased typically by a factor of 100 or more to force the flow to follow the direction of the tubes.

3.2 Connecting ducts design

As illustrated in Figure 2 the inflow duct is connected to the IPC exit and the outflow duct to the HPC entrance. Typical Mach number ranges for these are 0.25-0.35 and 0.45-0.55 respectively [21]. From the inflow duct entrance up to the tube stack, diffusion is needed to reduce the pressure loss through the intercooler. On the other hand an acceleration is needed in the outflow duct to match the required compressor entry condition. As Figure 4 illustrates, the outflow duct crosses through the middle of the inflow duct with an elliptical shape achieving a smooth area variation in the inflow duct. Initial work on an inflow, outflow configuration with the two ducts passing assymetrically was carried out. It was found difficult to keep the losses down in the diffusing inflow duct and the assymmetric concept was therefore abandoned.

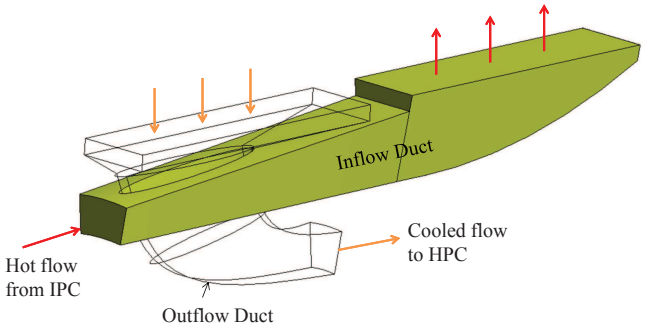

Fig. 4: Splitting inflow duct and outflow duct

Due to space constraints in the intersection region, the area increase needed from the IPC exit to the inflow tube stack will have to be made predominantly downstream of the intersection region. Separation therefore easily occurs just downstream of the inflow outflow intersection as seen from from Figure 5. To control the flow in this region an inflow guide vane is introduced as shown in Figure 6.

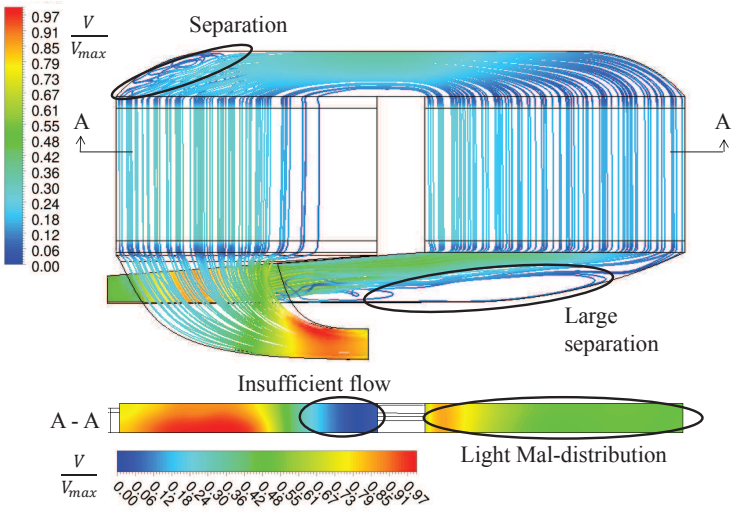

Fig. 5: Streamline plot of the internal side of the initial intercooler configuration, including velocity contours of the cross-sections of the porous domain

The velocity contour of the cross-section A-A of the porous domain represents the flow distribution in the porous media. The heavy flow mal-distribution in the outflow tube stack is a consequence of the design of the outflow duct. An aggressive

L turn is needed to guide the flow through a 90 degree change of direction. An improved outflow duct geometry is shown in Figure 6 below. The entry of the L duct was then extended further down in the axial direction, as compared to the original design shown in Figure5, to reduce the flow maldistribution.

In the crossover duct, there are actually two separations mixed together; one is induced by the upper wall boundary layer growth and the other one is induced by the side wall boundary layer growth. To address this a guide vane as illustrated in Figure 6 is applied to eliminate the former separation and a splitter is proposed to suppress the latter. Splitter 2 in the crossover duct is introduced to help the flow distribution by connecting the rich flow region of the inflow stack directly with the part of the outflow stack receiving insufficient flow. The insufficient or low-flow region of the outflow stack is indicated in Figure 5.

At the interfaces connecting the porous media domain and ducts, a sudden change in porosity occurs which means a sudden change in flow area and velocity, resulting in considerable pressure losses. A real intercooler tube inflow geometry would be designed with a smooth area transition. To simulate this, porous media parts are introduced, as illustrated in Figure 6, modelling tubes with a smoothly varying inlet diameter. The porosity in this region varies from 1.0 in the connecting ducts to the value applied in the intercooler tubes, which is estimated at 0.242 as given in Table 2.

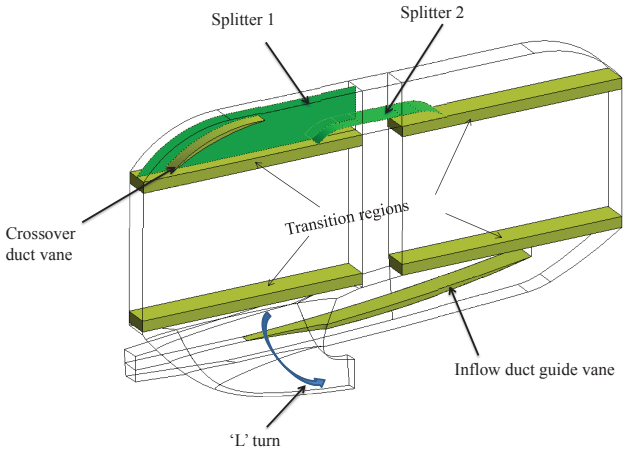

Fig. 6: Porous media modeled transition regions, guide vanes and splitters

3.3 CFD Analysis

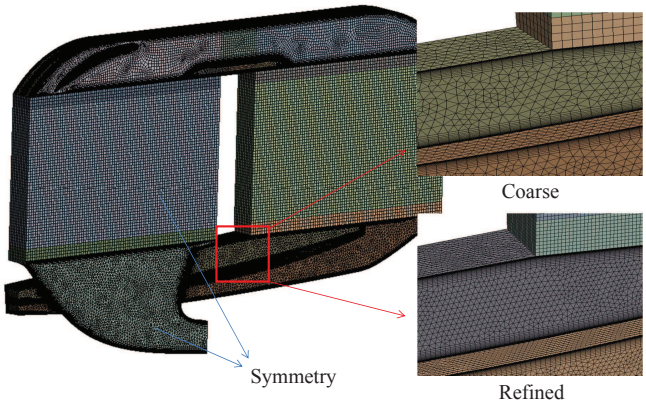

Fig. 7: Meshes for mesh resolution dependency investigation, coarse mesh (upper right), refined mesh (lower right)

A symmetry condition dividing the computational domain into two equal regions was used for the internal side simulations. The symmetry plane was located in the axial/radial plane. In order to investigate the mesh resolution dependency of the internal flow simulation, several meshes were tested. The mesh sizes evaluated are approximately a 2 million, a 3 million, a 4 million, and a 6 million element case generated with the same meshing strategy. The coarse mesh, 2 million cells, and a refined case, 6 million cells, can be seen in Figure 7. The resulting computational differences between these meshes are relatively modest showing good consistency with regards to flow separation and flow distribution. To minimise the computational load simulating different intercooler concepts and operating conditions, the 2 million mesh was used in

the design process and to establish the duct pressure loss correlations, while the 6 million mesh, was selected to verify its validity.

A structured mesh is generated in the porous media domain and an unstructured mesh is applied to the ducts. The value of y^+ is made less than 200 in the 2 million mesh case, and the automatic wall function in CFX SST model is applied. The boundary conditions are given in Table 2. These conditions represent the engine operation at take-off which is the most demanding operating condition of the intercooler in terms of heat transfer. At top of climb and mid cruise the mass flows and transferred heat are substantially lower, but so is the density giving relatively modest variations in flow Mach numbers.

	Boundary Condition Type	Boundary
Inlet	Total Pressure	706 kPa
Inlet	Total Temperature	556 K
Outlet	Pressure	610 kPa
Porous Media	Porosity	0.242
	Stream-wise directional quadratic resistance coefficient k'	8.5 kg/m^4
	Transverse directional loss multiplier	100

Table 2: Boundary conditions applied to the internal side simulations, take-off operating point

4 Results

4.1 External side results - transversal spacing variation

After some initial screening three cases with transversal distances $d_b = b$, $d_b = 2b$ and $d_b = 3b$, see Figure 3, were selected as a basis for the analysis. The three cases are denoted A, B and C respectively, and are illustrated schematically in the top of Figure 8. As will be discussed, case A and case C represent less favourable conditions whereas the case B represent a configuration with good friction and heat transfer characteristics.

Results of case A, B, and C are shown in Figure 8. For a given average Reynolds number the Colburn j factor and friction factor f generally show an increasing trend with increasing spacing d_b. This is consistent with the general trends that have been observed for circular tube stacks by for instance Kays and London [15] and by Halici and Taymaz [22]. However, in the high Reynolds number region of case A, the friction factor increases rapidly with increasing Reynolds number and the last point almost meets the curve of case C. In case A, the tube passage form convergent divergent ducts, with an area ratio considerably larger than in case B and C. As the Mach number increases through the tube array, it reaches a relatively high value entering the last tube column. The small area, increase in stagnation temperature and reduction of stagnation pressure cause the flow to choke in the smallest passage, and then accelerate further into the divergent part where a shock occurs.

The generally observed trend of a reducing friction factor as d_b decreases can be interpreted in more detail by analyzing the skin friction and pressure drag components of the friction factor. Figure 9 gives the pressure coefficient C_p and the friction coefficient C_f as defined by:

$$C_f = \frac{\tau}{0.5\rho_\infty (u_\infty)^2} \tag{5}$$

$$C_p = \frac{p - p_\infty}{0.5\rho_\infty (u_\infty)^2} \tag{6}$$

where, τ is the local wall shear stress, p is the local pressure, u is the average axial velocity. The index ∞ represents the free stream value which is computed at a plane where the maximum thickness of the ellipse is located. The 18th tube column was selected to illustrate the C_p and C_f distributions, since it represents a well developed flow with negligible influence of the outflow conditions.

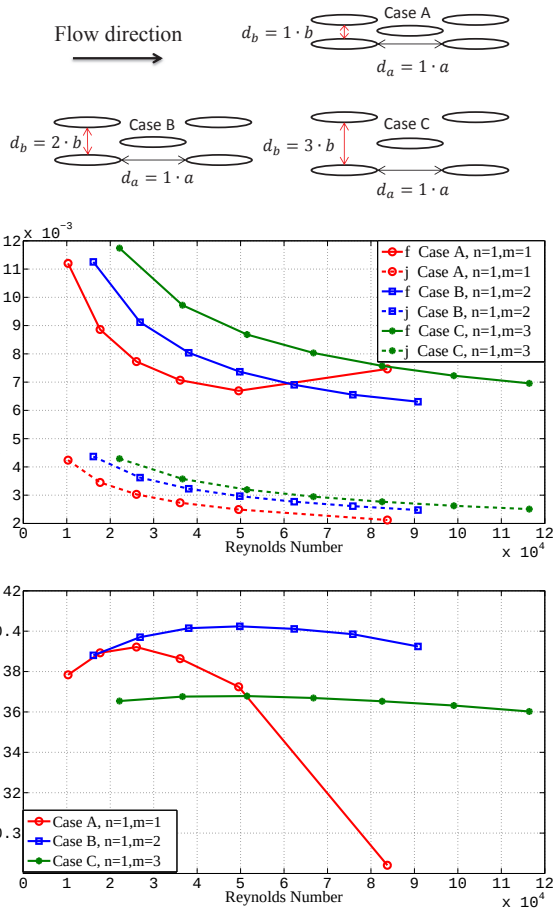

Fig. 8: For the cases with varying d_b: Colburn j factor and friction factor f (Top) , Ratio between j and f (Bottom)

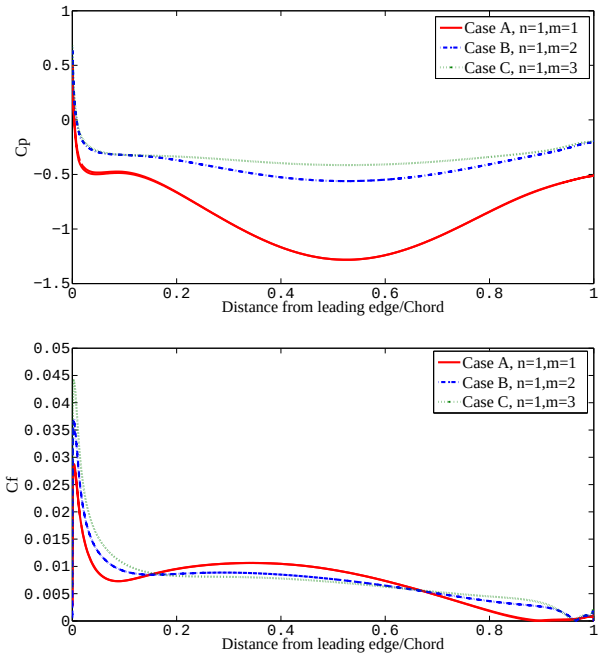

Fig. 9: Skin friction coefficient C_f (Top) and pressure coefficient C_p (Bottom) Distribution around the 18^{th} tube, for the cases with varying d_b and an average Reynolds number of $50,000$

As illustrated in the friction coefficient C_f plot of Figure 9, at the region near the leading edge of the tube, the C_f value increases with increasing transversal distance d_b. The Colburn j factor shows a similar trend as is generally expected from

the Reynolds analogy [23]. However, as was discussed previously the friction factor, is composed of both the friction and pressure drag. Hence the effect of C_p must be considered when friction factor is analysed. Obviously from the C_p plot, case A which has the smallest transversal spacing shows the largest pressure gradient, which in turn causes the largest pressure drag. In the low Reynolds number region, the friction loss would dominate the friction factor, which is the reason for observing a similar trend in the j factor. However, when the Reynolds number increases, the pressure drag starts to have a larger impact on the friction factor, which is captured by a moderate convergence of the friction factor curves as illustrated in Figure 8. As dicussed above, the high Reynolds number range of case A is primarily governed by transonic effects and the development of shocks. The calculated ratio of the Colburn j factor to the friction coefficient f, as shown in the lower part of Figure 8, gives a considerably higher ratio for case B than for case C. On average an almost 10% increase in Colburn factor to friction coefficient ratio is observed. Note that case B, having a smaller transversal spacing than case C, also has the advantage of reducing the volume requirement for the intercooler. Case B is therefore selected as a starting point for the analysis of the axial spacing parameter d_a, as presented below.

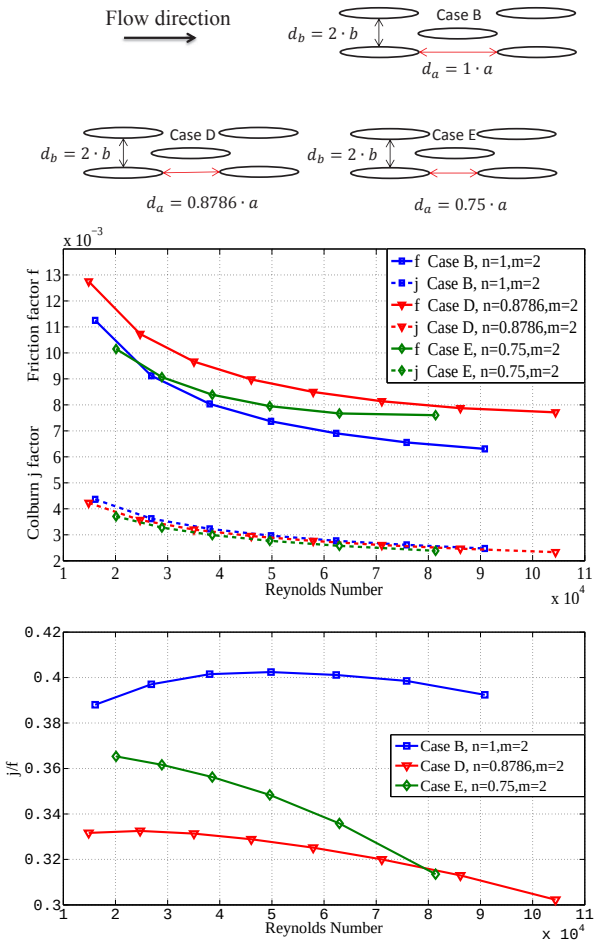

Fig. 10: For the cases with varying d_a:Colburn j factor and friction factor f (Top) , Ratio between j and f (Bottom)

4.2 External side results - axial spacing variation

For analyzing the effect of varying axial spacing, three cases are selected based on the tube ellipse major axis a having $d_a = a$, $d_a = 0.8786a$ and $d_a = 0.75a$ as illustrated in Figure 10. These cases are labelled B, D and E respectively, where case B was introduced already as part of the previous section. The value of n in case D (0.8786) is the particular case where the two minimum free-flow areas in flow passage over the ellipse are equal, $d_b = 2d$, as illustrated in Figure 3. This particular case is selected with the intent to keep the flow path area variation minimal.

The axial spacing parametric study generally shows a greater complexity than observed for the transversal cases. With a smaller axial spacing d_a, as represented by case D in Figure 10, a higher friction factor than for case B is observed but no significant difference in the Colburn j factor is noted. However, for an even smaller axial spacing the friction factor drops back as seen in case E, although in the high Reynolds number region the friction factor tends to be as high as case D, whereas the heat transfer coefficient is actually somewhat lower. The reason for the unexpected drop in friction factor, as the distance

is reduced further from case D to case E, is that the adjacent ellipses start to overlap and create local acceleration/deceleration zones. This is seen from the Mach number contours in Figure 11. The local acceleration zones surpress boundary layer growth and increase skin friction locally, as seen from the C_f plot of Figure 12. However the rapid growth of the boundary layer in the retardation zone over the top of the ellipse reduces skin friction over a large part of the surface. Overall this results in a reduction in the friction drag. The pressure drag is strongly affected by the hump in C_p occurring in the rear acceleration zone. Hence the pressure drag of case E will grow more strongly with Reynolds number than for the two other cases and this effect will dominate for a sufficiently large Re-number. For sufficiently low Re-number case E will show the lowest skin friction due to the favourable friction drag.

With an approximately constant area through the flow field, case D obtains a relatively flat C_p contour, but two small humps can still be observed. The first small hump starts from around 10% of the chord resulting in a decrease in skin friction and increase in pressure drag, and the second small hump close to the end increases both the skin friction and pressure drag. Thus, the effects on the skin friction cancel out which gives quite the same heat transfer capability as in case B. From the ratio between the j factor and friction factor plots, case B still promises to be the most favourable configuration, almost 20% better than case D. Case E is abandoned due to the risk of excessive pressure loss in higher Reynolds number regions. However, with a resulting 14% reduction in axial length, case D gives a better engine integration capability and this configuration is therefore chosen as the starting point for the internal flow simulations. The optimal choice on geometry parameters ultimately depends on the engine requirements and can not be decided at the intercooler component level. For this reason all five cases analyzed (A, B, C, D and E) are provided as part of the correlation section.

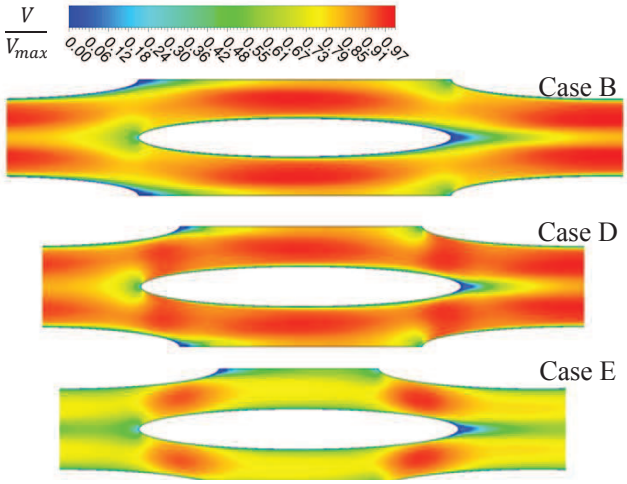

Fig. 11: Mach number variation around the 18^{th} tube column at inflow Mach number of 0.2, Case B (Top), Case D (Middle) and Case E (Bottom)

4.3 Internal side results

In this section the following sequence of duct design cases, as illustrated in Figure 6, are analysed.

Case A: concept with inflow duct guide vane only;
Case B: Case A with improved outflow duct 'L' turn design and increased inflow duct area;
Case C: Case B with 'Splitter 1' included;
Case D: Case C with crossover duct vane included;
Case E: final design solution. Case D with 'Splitter 2' included.

A flow visualization of Case A is shown in Figure 13, from which it can be seen that the flow distribution pattern is greatly improved in the inflow tube stack. The separation in the inflow duct is also suppressed to a very low level, which gives a substantially reduced pressure loss. However, as the inflow passes the area where the inflow and outflow ducts intersect the available flow area has to be reduced. This leads to a local acceleration and then a relatively rapid deceleration over the leading edge area of the inflow guide vane. The associated adverse pressure gradient contributes to generate a vortex structure that extends over almost half of the chord length of the upper side of the inflow guide vane. This vortex is actually helping the flow distribution by suppressing the flow separation along the vane, but it contributes to a locally increased pressure loss. The net pressure loss for the inflow duct is however reduced as is seen in Table 3. Still, an increased area in the inflow outflow intersection region was believed to be effective in order to reduce the pressure loss in the inflow duct. As part of Case B, this was achieved by increasing the inflow duct height as illustrated in Figure 14.

With the improved L turn design of case B, see Figure 14, it can be seen that the flow distribution of the outflow tube stack has been improved, but additional modifications are still needed to optimise the flow in the L turn and to improve the

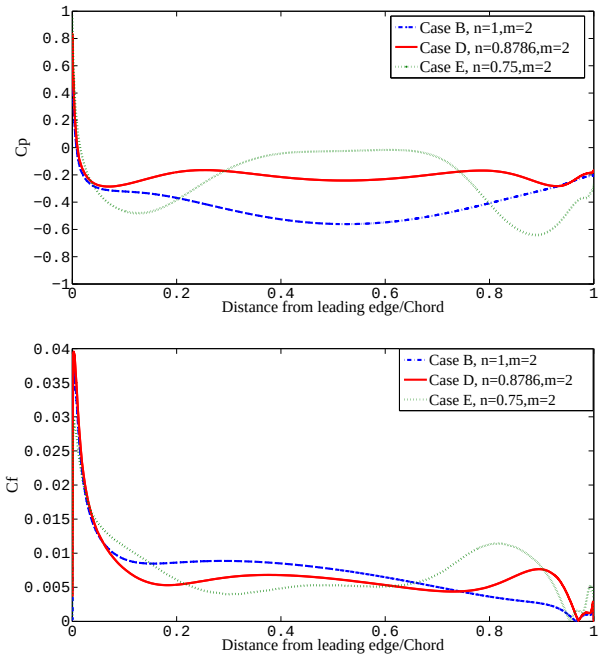

Fig. 12: Skin friction coefficient C_f (Top) and pressure coefficient C_p (Bottom) distribution around the 18^{th} tube, for the cases with varying d_a and average Reynolds number of $50,000$

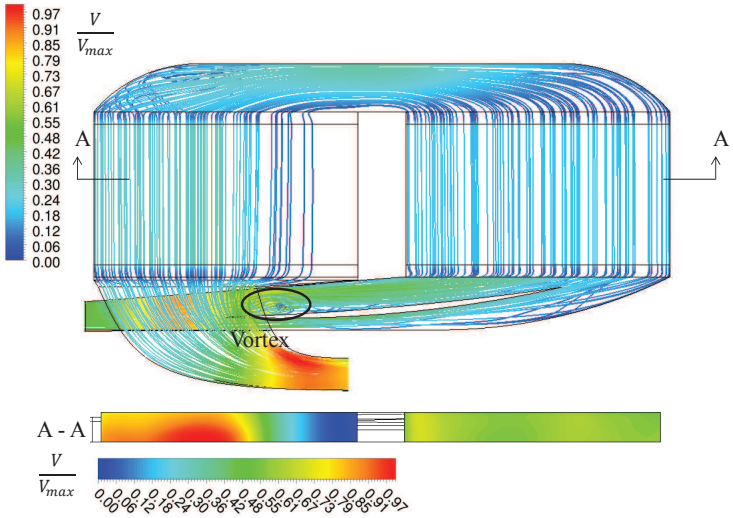

Fig. 13: Streamline plot of the internal side of the intercooler and velocity contour of cross-section of porous domain, case A

flow distribution of the outflow tube stack. The increased inflow duct area makes the flow distribution in the inflow tube stack worse. Although the vortex is now eliminated the flow starts to separate from the upper side of the vane. Still, the contribution of the increased inflow duct area leads to a remarkable improvement in the inflow duct pressure loss.

In the crossover duct a separation can be observed from the streamline plot in the top of Figure 15 as indicated by the encircled region. To reduce the pressure loss associated with this separation, a splitter ('Splitter 1') and a crossover duct vane are introduced. With only the 'Splitter 1' (Case C), the separation caused by the side wall boundary layer growth is suppressed, but a large separation from the upper wall is observed, see Case C of Figure 15. The addition of the cross over duct guide vase (Case D) largely eliminates the separation in the crossover duct as shown in the bottom of Figure 15. Although the separation is suppressed the use of crossover duct vane also increases the wetted area and hence there is no further reduction in pressure loss when both are applied, as seen from Table 3. However, a slight improvement in pressure loss in the tube stacks is observed. In total the introduction of 'Splitter 1' and the crossover duct vane reduces the pressure total loss of the intercooler and some pressure loss is re-distributed to the intercooler tube stacks. This re-distribution is believed to be beneficial since it may contribute to increasing the heat transfer capability of the intercooler. Furthermore, by comparing the total pressure loss incurred in the inflow duct, it can be seen that the introduction of the 'Splitter 1' reduces the pressure loss from 1.96% to 1.73% due to the re-distribution of the flow in the tubes stacks.

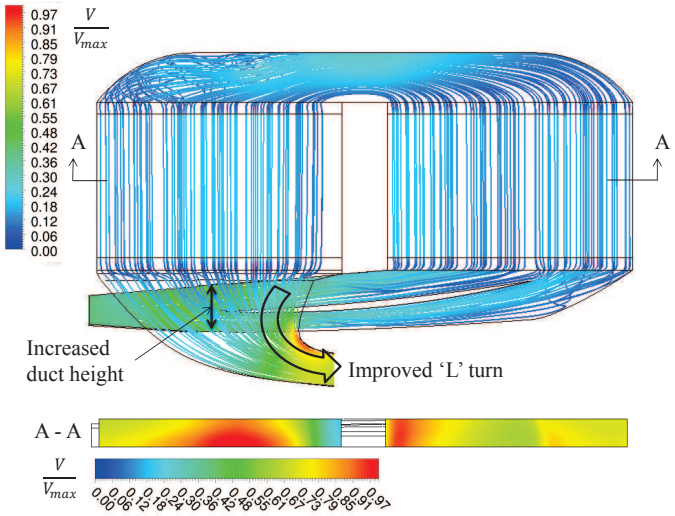

Fig. 14: Streamline plot of the internal side of the intercooler and velocity contour of cross-section of porous domain, case B

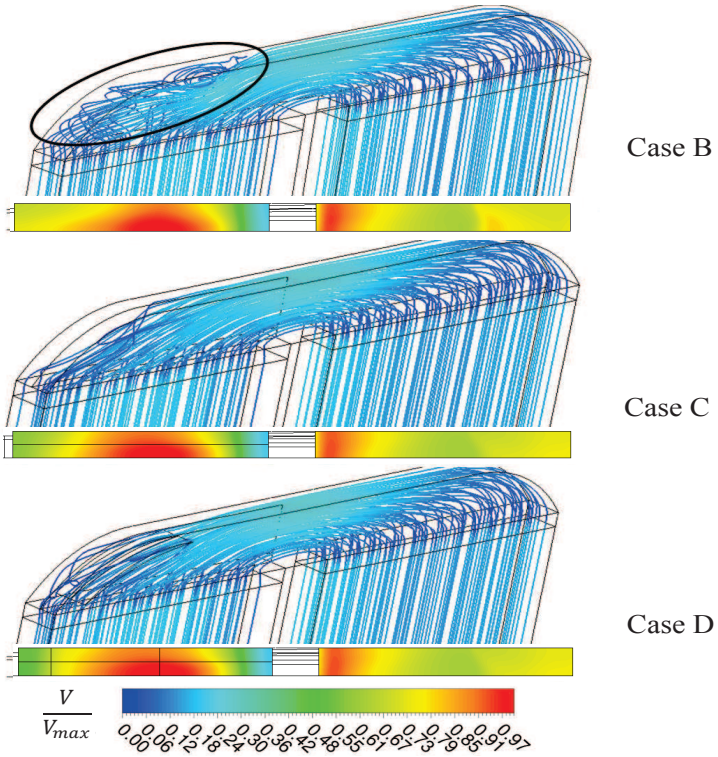

Fig. 15: Streamline plot of the crossover duct and velocity contour of cross-section of porous domain with corresponding cases B, C and D

The 'Splitter 1' and crossover duct vane did not contribute to improving the tube stack flow distribution. Actually, apart from the flow maldistribution related to the corner separation of the crossover duct, the flow distribution in the intercooler tube stacks has degraded. From the A-A cross section velocity contours presented in Figure 15, it can be seen that there are still some regions with flow maldistribution. The final design modification studied in this paper, through the inclusion of 'Splitter 2' (case E), was intended to balance the flow by creating a channel directly connecting the rich flow part of inflow tube stack with the poor flow part of outflow tube stack. The result is shown in Figure 16 below, which shows a substantial improvement in the inflow tube stack flow distribution. The net pressure loss drops slightly as indicated in Table 3. In summary, the successive improvement of the original configuration leading up to the definition of Case E has resulted in a relatively well distributed intercooler flow pattern as seen from Figure 16.

	Original	Case A	Case B	Case C	Case D	Case E
Inflow duct	3.36%	2.95%	1.96%	1.73%	1.73%	1.73%
Outflow duct	1.02%	1.08%	0.68%	0.69%	0.69%	0.70%
Crossover duct	0.24%	0.29%	0.27%	0.19%	0.19%	0.19%
Tube stacks (Porous media)	2.91%	2.78%	2.30%	2.38%	2.36%	2.32%
Net pressure loss	7.53%	7.10%	5.21%	4.99%	4.97%	4.94%

Table 3: Summary of internal side pressure loss distributions

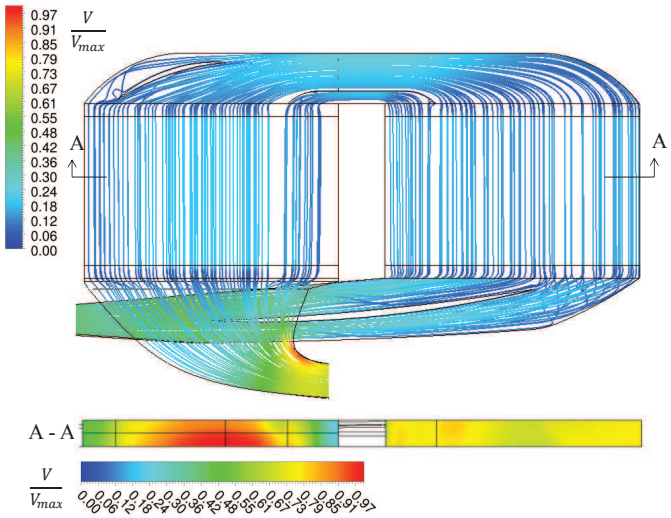

Fig. 16: Streamline plot of the internal side of the intercooler and velocity contour of cross-section of porous domain, case E

4.4 Correlations for performance modeling

To provide a reduced order model suitable for conceptual design of intercooled aero engines, a set of correlations for the studied two-pass cross flow configuration must be established. It should be noted that the provided correlations are valid as part of a scaling procedure usually implemented when conceptual gas turbine design is being performed.

Although the ducts and tube stacks were simulated connected to each other, the correlations for the internal side are given separately. The tube stack modeling is obtained from existing correlations, where both the heat transfer [24] and pressure drop characteristics [20] are included. Note that the reduction in temperature as the internal flow goes through the intercooler should be accounted for when evaluating the internal pressure loss. The reduction in temperature reduces the internal flow Mach numbers which in turn leads to a reduction in pressure loss.

Inflow duct (Reynolds number based on the inflow duct inlet condition, valid in the range of 500,000 to 1,400,000, and the largest deviation from CFD results in this correlation is 0.81%.)

$$k_{inflow\,duct} = \frac{(p_{out} - p_{in})}{(P_{in} - p_{in})} = -1.626 \times 10^{9} Re^{-1.837} + 0.5513$$

Tube stack (Reynolds number based on the hydraulic diameter of the elliptical tube)

$$\frac{1}{\sqrt{k_{tube}}} = -1.8 \log_{10}(6.9/Re + (\varepsilon/D/3.7)^{1.11})$$

$$Nu = \frac{(k_{tube}/8.0)(Re - 1000)Pr}{1 + 12.7\sqrt{(k_{tube}/8.0)}(Pr^{2/3} - 1)}$$

Crossover duct (Reynolds number based on the crossover duct inlet condition, valid in the range of 100,000 to 350,000,

and the largest deviation from CFD results in this correlation is 0.78%.)

$$k_{crossover\,duct} = \frac{(p_{in} - p_{out})}{(P_{in} - p_{in})} = 3.128 \times 10^{-7} Re + 10.1$$

Outflow duct (Reynolds number based on the outflow duct outlet condition, valid in the range of 1,500,000 to 5,500,000, and the largest deviation from CFD results in this correlation is 0.72%.)

$$k_{out\,flow\,duct} = \frac{(P_{in} - P_{out})}{(P_{out} - p_{out})} = 1.939 \times 10^{11} Re^{-2.1} + 0.08107$$

where in the correlations above, the k is the loss factor with the subscript representing which duct it applies to; p is the static pressure, P is the total pressure, while 'in' and 'out' subscript represents the inlet and outlet of the duct respectively; D is the hydraulic diameter of the elliptical tube; ε is the roughness of the tube wall, the value of 0.002 *mm* is assumed here.

External side (see definition in equation (1) and (3), the largest deviation from CFD data in this correlation is 0.90%.)

A	$j = 0.00397e^{(-1.144 \cdot 10^{-4} \cdot Re)} + 0.003159e^{(-4.427 \cdot 10^{-6} \cdot Re)}$
	$f = 0.01193e^{(-1.305 \cdot 10^{-4} \cdot Re)} + 0.008503e^{(-5.292 \cdot 10^{-6} \cdot Re)}$
B	$j = 0.003469e^{(-7.117 \cdot 10^{-5} \cdot Re)} + 0.003461e^{(-3.793 \cdot 10^{-6} \cdot Re)}$
	$f = 0.01044e^{(-6.806 \cdot 10^{-5} \cdot Re)} + 0.008109e^{(-2.908 \cdot 10^{-6} \cdot Re)}$
C	$j = 0.003402e^{(-5.241 \cdot 10^{-5} \cdot Re)} + 0.003417e^{(-2.739 \cdot 10^{-6} \cdot Re)}$
	$f = 0.009905e^{(-5.162 \cdot 10^{-5} \cdot Re)} + 0.009003e^{(-2.303 \cdot 10^{-6} \cdot Re)}$
D	$j = 0.002967e^{(-6.734 \cdot 10^{-5} \cdot Re)} + 0.00329e^{(-3.385 \cdot 10^{-6} \cdot Re)}$
	$f = 0.009581e^{(-6.043 \cdot 10^{-5} \cdot Re)} + 0.009015e^{(-1.617 \cdot 10^{-6} \cdot Re)}$
E	$j = 0.003328e^{(-8.018 \cdot 10^{-5} \cdot Re)} + 0.003389e^{(-4.338 \cdot 10^{-6} \cdot Re)}$
	$f = 0.009929e^{(-6.404 \cdot 10^{-5} \cdot Re)} + 0.007792e^{(-6.163 \cdot 10^{-7} \cdot Re)}$

Table 4: External side correlations

5 Discussion and conclusion

Optimizing an intercooled turbofan engine requires finding a cycle that maximizes the benefits of the intercooling technology for the aircraft operation intended. An intercooler may help to lower the high pressure compressor exit temperatures and thereby reduce cooling air temperatures and the cooling air mass flow requirement, as well as contribute to reduce NO_x emissions. The reduced compressor exit temperature may also provide a path to radically increase the overall pressure ratio of the engine cycle. Alternatively intercooling may be used to establish a power plant with an increased specific power to allow a reduction in engine size or to allow increasing the engine bypass ratio. Hence, a range of design philosophies may be used to maximize the benefits of intercooling and consequently an optimal intercooler aerodynamic design must be optimal with respect to the design philosophy chosen. For this reason it was decided to include correlations that cover a range of realistic operating conditions, allowing the concept to be evaluated as part of an engine integrated design optimization.

In general, the tubular two-pass cross flow intercooler is believed to provide a relatively low internal pressure loss comparing to other aero engine intercooler design concepts. The design is also expected to have a relatively favourable weight scaling with increasing pressure due to the tubular design. The heat transfer characteristics provide a good but not extreme heat exchange capability at a reasonable level of external pressure losses. In addition, the two-pass cross flow elliptical tube intercooler is expected to be relatively easy to manufacture as techniques to cost effectively design lightweight relatively stiff tube geometries exist [12].

6 Acknowledgement

This work is financially supported by the E.U. under the "LEMCOTEC - Low Emissions Core-Engine Technologies, a Collaborative Project co-funded by the European Commission within the Seventh Framework Programme (2007-2013) under the Grant Agreement n 283216.

References

[1] McDonald, C., Massardo, A., Rodgers, C., and Stone, A., 2008. "Recuperated Gas Turbine Aeroengines, Part I: Early Development Activites". *Aircraft Engineering and Aerospace Technology: An International Journal,* **80**(2), pp. 139–157.

[2] McDonald, C., Massardo, A., Rodgers, C., and Stone, A., 2008. "Recuperated Gas Turbine Aeroengines, Part II: Engine Design Studies Following Early Development Testing". *Aircraft Engineering and Aerospace Technology: An International Journal,* **80**(3), pp. 280–294.

[3] McDonald, C., Massardo, A., Rodgers, C., and Stone, A., 2008. "Recuperated Gas Turbine Aeroengines, Part III: Engine Concepts for Reduced Emissions, Lower Fuel Consumption, and Noise Abatement". *Aircraft Engineering and Aerospace Technology: An International Journal,* **80**(3), pp. 408–426.

[4] Kyprianidis, K., Grönstedt, T., Ogaji, S. O. T., Pilidis, P., and Singh, R., 2011. "Assessment of Future Aero-Engine Designs with Intercooled and Intercooled Recuperated Cores". *Journal of Engineering for Gas Turbines and Power,* **133**(11), Jan.

[5] Wilfert, G., Sieber, J., Rolt, A., Baker, N., Touyeras, A., and Colantouni, S., 2007. "New Enviromentally Friendly Aero Engine Core Concepts". *The 18th International Symposium on Air Breathing Engines, Beijing, China, ISABE-2007-1120*, Sep.

[6] Lundbladh, A., and Sjunnesson, A., 2003. "Heat Exchanger Weight and Efficiency Impact on Jet Engine Transport Applications". *The 16th International Symposium on Air Breathing Engines, Cleveland, Ohio, ISABE-2003-1122*, Sep.

[7] Xu, L., 2011. "Analysis and Evaluation of Innovative Aero Engine Core Concepts". PhD Thesis, Chalmers University of Technology, Gothernburg, Sweden.

[8] Walker, A. D., Regunath, G. S., Carrotte, J. F., and Denman, P. A., 2012. "Intercooled Aero-Gas-Turbine Duct Aerodynamics: Core Air Delivery Ducts". *Journal of Propulsion and Power,* **28**(6), Nov.-Dec.

[9] Walker, A. D., Carrotte, J. F., and Rolt, A. M., 2009. "Duct Aerodynamics for Intercooled Aero Gas Turbines: Constraints, Concepts and Design Methodology". *Proceedings of ASME Turbo Expo 2009: Power for Land, Sea and Air, GT2009-59612*, June 8-12.

[10] Xu, L., and Grönstedt, T., 2009. "Design and Analysis of an Intercooled Turbofan Engine". *Journal of Engineering for Gas Turbines and Power,* **132**, Nov.

[11] Khan, W. A., Culham, J. R., and Yovanovich, M. M., 2005. "Fluid Flow Around and Heat Transfer from Elliptical Cylinders". *Journal of Thermophysics and Heat Transfer,* **19**(2), April-June.

[12] Grieb, H., and Schlosser, W., 1988. "Shaped Tube with Elliptical Cross-section for Tubular Heat Exchangers and a Method for Their Manufacture". *United States Patent*(4766953), August.

[13] ANSYS Inc., 2006. Innovative Turbulence Modeling: SST Model in ANSYS CFX. Technical report, ANSYS Inc., Canonsburg, PA.

[14] Menter, F., Ferreira, J., Esch, T., and Konno, B., 2003. "The SST Turbulence Model with Improved Wall Treatment for Heat Transfer Predictions in Gas Turbines". *Proceeding of the International Gas Turbine Congress, Tokyo*, Nov.

[15] Kays, W. M., and London, A. L., 1964. *Compact Heat Exchanger, 2nd ed.* McGraw-Hill, ISBN 07-033391-2.

[16] Kritikos, K., Albanakis, C., Missirlis, D., Vlahostergios, Z., Goulas, A., and Storm, P., 2010. "Investigation of the Thermal Efficiency of a Staggered Elliptic-tube Heat Exchanger for Aeroengine Applications". *Applied Thermal Engineering,* **30**, pp. 134–142.

[17] Missirlis, D., Donnerhack, S., Seite, O., Albanakis, C., Sideridis, A., Yakinthos, K., and Goulas, A., 2010. "Numerical Development of a Heat Transfer and Pressure Drop Porosity Model for a Heat Exchanger for Aeroengine Applications". *Applied Thermal Engineering,* **30**, pp. 1341–1350.

[18] Missirlis, D., Yakinthos, K., Palikaras, A., Katheder, K., and Goulas, A., 2005. "Experimental and Numerical Investigation of the Flow Field through a Heat Exchanger for Aeroengine Applications". *Int. J.Heat and Fluid Flow,* **26**, pp. 440–458.

[19] ANSYS Ltd., 2010. *Ansys CFX Help*, release 12.0 ed. ANSYS Ltd.

[20] Haaland, S. E., 1983. "Simple and explicit formulas for the friction factor in turbulent pipe flow". *J. Fluids Eng.,* **105**(1), pp. 89–90.

[21] Grieb, H., 2004. *Projektierung von Turboflugtriebwerken*. Birkhäuser, ISBN 3-7643-6023-2.

[22] Halici, F., and Taymaz, I., 2006. "Experimental Study of the Airside Performance of Tube Row Spacing in Finned Tube Heat Exchangers". *Heat Mass Transfer,* **42**, pp. 817–822.

[23] Eckert, E. R. G., and Drake, R. M., 1972. *Analysis of Heat and Mass Transfer*. McGraw-Hill, New York.

[24] Gnielinski, V., 1976. "New equations for heat and mass transfer in turbulent pipe and channel flow". *International Chemical Engineering,* **16**, pp. 359–368.

Paper B

Zhao, X., Grönstedt, T. and Kyprianidis, K., **Assessment of The Performance Potential for a Two-pass Cross Flow Intercooler for Aero Engine Applications**. The 21th ISABE conference, September 9-13, 2013, Busan, South Korea.

ISABE-2013-1215

ASSESSMENT OF THE PERFORMANCE POTENTIAL FOR A TWO-PASS CROSS FLOW INTERCOOLER FOR AERO ENGINE APPLICATIONS

Xin Zhao
Ph.D. student
Chalmers University of Technology
SE-412 96 Göteborg, Sweden
xin.zhao@chalmers.se

Tomas Grönstedt
Professor
Chalmers University of Technology
SE-412 96 Göteborg, Sweden
tomas.gronstedt@chalmers.se

Konstantinos G. Kyprianidis
Rolls-Royce Defence Aerospace
Bristol, United Kingdom
konstantinos.kyprianidis@rolls-royce.com

Abstract

The performance potential for a two-pass cross flow intercooler has been estimated through an analysis of a long range mission for a geared turbofan engine. The application of a set of CFD based correlations allows the simultaneous coupled optimization of the intercooler conceptual design parameters and the engine design. The coolant air for the intercooler is ejected through a separate variable exhaust nozzle which is used to optimize the engine performance in cruise. By comparing the optimized intercooled geared engine with an optimized advanced non-intercooled geared engine, a reduction of 4.8% fuel burn is observed.

Nomenclature

a	Major axis length of the elliptical tube
b	Minor axis length of the elliptical tube
D	Diameter
D_h	Hydraulic diameter of any internal passage
f	Friction factor
h	Heat transfer coefficient
j	Colburn j factor
K	Loss coefficient for ducts
k_{loss}	Tube internal loss coefficient
$\dot{m}$	Mass flow rate
p	Static pressure
P	Total pressure
T	Temperature
ρ	Density
ε	Roughness of the tube wall
μ	Dynamic viscosity
η	Polytropic efficiency
k	Thermal conductivity of air
Re	Reynolds number
Pr	Prantdl number
Nu	Nusselt number
St	Stanton number
BPR	Bypass ratio
FPR	Fan pressure ratio
HPC	High pressure compressor
IPC	Intermediate pressure Compressor
LPT	Low pressure turbine
OPR	Overall pressure ratio
PR	Pressure ratio
SFC	Specific fuel consumption
SFN	Specific thrust
TOC	Top of climb
NEWAC	New Aero Engine Core Concepts
LEMCOTEC	Low Emissions Core-Engine Technologies

Introduction

Intercoolers have recently received a considerable attention as a means to improve aero engine efficiency, in particular within the European research projects NEWAC and LEMCOTEC [1-8], and within the US N+3 project [9]. Intercoolers have the potential to improve engine SFC, ease the design of an efficient turbine cooling system by reducing compressor exit temperatures and hence cooling air temperatures, as well as reducing NO_x emissions. Intercooling may also provide benefits by increasing the specific output of the engine core and therefore reduce total engine weight.

Although the design of compact heat exchangers is a mature field and a wealth of design data exists [10], the availability of data directly applicable to aero engine performance studies is quite limited. Aero engine performance is strongly influenced by the weight and volume of the intercooler and the pressure losses incurred from its integration as well as the design strategy employed. Here the term design strategy refers to the sizing of the intercooler related to the mission. Within this work it is argued that it is beneficial to provide a relatively large amount of intercooling at take-off to allow for a compact engine design with a high OPR and a reduced cooling flow need. In cruise on the other hand, it is beneficial to reduce the intercooling by use of a variable intercooler exhaust nozzle, indicated in the lower part of Figure 1, to establish an optimum between intercooling and incurred pressure losses.

Another design issue that has to be addressed is to decide where in the compression process the intercooling should be introduced. An early introduction is favourable from a thermodynamic perspective whereas a later introduction will reduce the intercooler pressure losses, weight and simplify its integration by reducing the intercooler volume requirement.

Finally, the choice of the intercooler configuration itself has a decisive impact on the performance that can be achieved by an intercooled engine. It is argued here that there is a need for performance estimates that realistically represent intercoolers designed and optimized for aero engine applications.

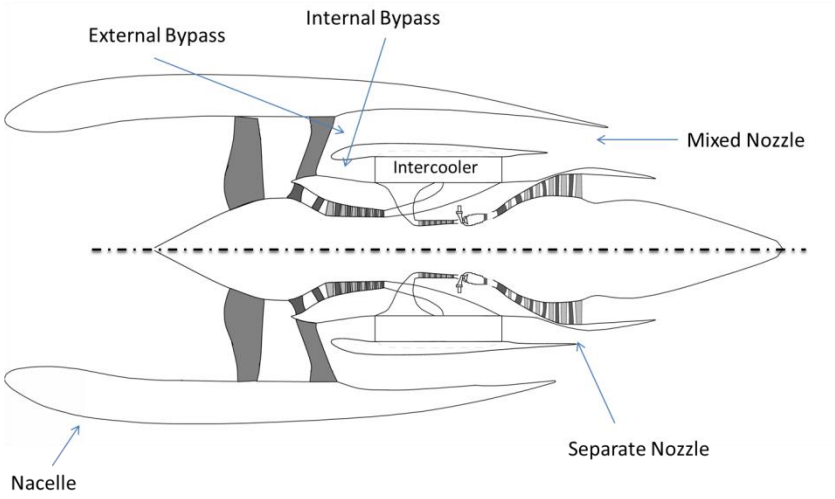

Figure 1 Intercooled engine impression [11]

This will enable engine performance in a more realistic way than can be achieved by assuming pressure loss levels or by applying simplified correlations.

The general configuration of the two-pass cross flow intercooler can be seen in Figure 2 below. Flow exiting an intermediate compressor or high speed booster enters the inflow duct through which it is diffused. The flow then enters the first stack of a tubular heat exchanger located downstream in the cooling flow direction, returns to an upstream tubular heat exchanger and then continues to an accelerating duct leading to the high pressure compressor entrance. Bypass air flows over the external surfaces of the two tubular stacks to achieve the sought intercooling. This paper extends the previous work on this concept [4, 11] by considering an involute spiral configuration for the intercooler tubes.

CFD studies for the re-designed concept was used to obtain a set of correlations which were used to evaluate the performance of a high bypass ratio intercooled geared turbofan.

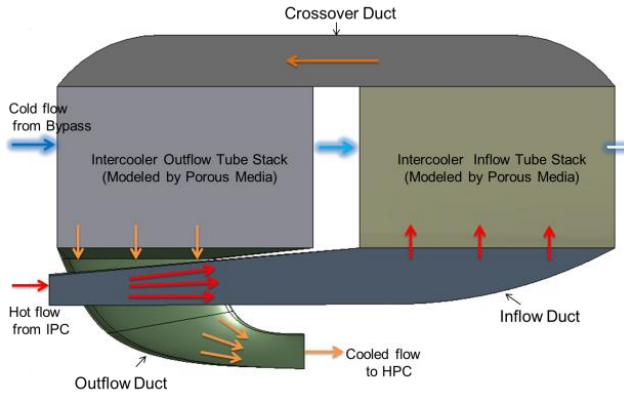

Figure 2 Two-pass cross flow intercooler impression

For a geared turbofan the LPT has a higher rotational speed than in the conventional turbofan, for which the rotational speed of the low pressure shaft is limited by the fan tip speed. For the LPT, an increased rotational speed gives a lower blade loading, higher efficiency and allows the use of fewer stages. Hence, the bypass ratio can be ultra-high without an excessive number of LPT stages. The increased shaft speed also allows for a smaller shaft diameter that makes it possible to integrate the high pressure compressor at a lower radius. This increases last stage blade height which is particularly critical for intercooled engines, which are expected to gain some of their benefits from a substantially increased OPR.

Intercooler Modelling

The correlations of the two-pass cross flow intercooler are divided into a correlation for the internal hot side connecting ducts and tubes, as well as characteristics for the external cold side staggered tubes. The general staggered tube configuration, that is the cross-section of the tube stack, can be seen from Figure 3 and the general parameters for this tube arrangement are defined in Table *1*.

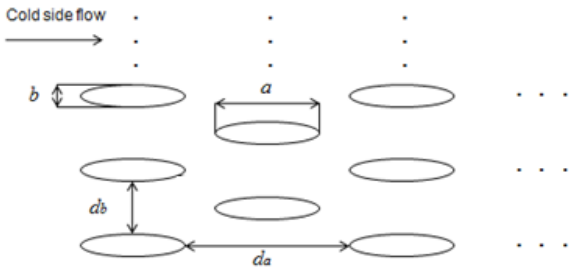

Figure 3 Intercooler external side configuration

a/b	8
d_a	a
d_b	2 b

Table 1 Tubes arrangement parameters

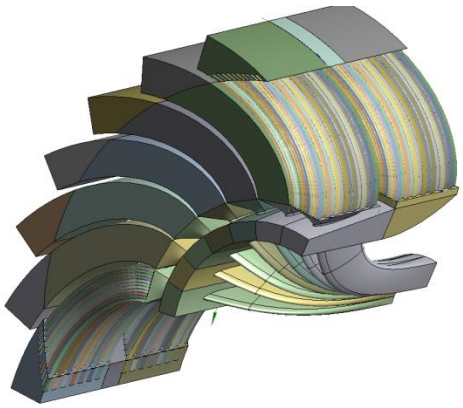

Figure 4 Involute spiral tubes configuration

An involute spiral tube configuration design is adopted for the tube stack. As seen from Figure 4 this concept gives a good utilization of the space available.

Correlations

Internal Core Side

Inflow duct (Reynolds number is based on the inflow duct inlet condition. Correlation is valid in the range of 500,000 to 1,400,000. The largest deviation from CFD data in this correlation is 0.81%):

$$K_{inflow\_duct} = -1.626 \times 10^{9} Re^{-1.837} + 0.5513$$

$$K_{inflow\_duct} = \frac{p_{out} - p_{in}}{P_{in} - p_{in}}$$

Tubes (Pressure loss correlation from [12]. Heat transfer correlation from [13]):

$$\frac{1}{\sqrt{k_{loss}}} = -1.8\log_{10}\left(\frac{6.9}{Re} + \left(\frac{\varepsilon}{D_h}/3.7\right)^{1.11}\right)$$

$$Nu = \frac{(k_{loss}/8.0)(Re - 1000)Pr}{1 + 12.7\sqrt{\left(\frac{k_{loss}}{8.0}\right)}\left(Pr^{\frac{2}{3}} - 1\right)}$$

Crossover duct (Reynolds number is based on the crossover duct inlet condition. Correlation is valid in the range of 100,000 to 350,000. The largest deviation from CFD data in this correlation is 0.78%):

$$K_{crossover\_duct} = 3.128 \times 10^{-7} Re + 10.1$$

$$K_{crossover\_duct} = \frac{p_{in} - p_{out}}{P_{in} - p_{in}}$$

Outflow duct (Reynolds number is based on the outflow duct outlet condition. The correlation is valid in the range of 1,500,000 to 5,500,000. The largest deviation from CFD data in this correlation is 0.72%):

$$K_{outflow\_duct} = 1.939 \times 10^{11} Re^{-2.1} + 0.08107$$

$$K_{outflow\_duct} = \frac{P_{out} - P_{in}}{P_{out} - p_{out}}$$

In the correlations above, p is the static pressure and P is the total pressure, while 'in' and 'out' subscripts represent the inlet and outlet of the duct respectively; ε is the roughness of the tube wall, (a value of 0.002 mm is assumed here). The hydraulic diameter of the ducts and the tube are used to calculate the Reynolds number in the corresponding correlations.

External Cold Side

The Colburn j factor is used here which is the dimensionless heat transfer coefficient as defined in [10]:

$$j = St \cdot Pr^{2/3} = \frac{Nu}{Re \cdot Pr} Pr^{2/3}$$

The Nusselt number, the Reynolds number and the related hydraulic diameter used in the external cold side correlations are calculated as:

$$D_h = \frac{4A_c L}{A_w}$$

$$Nu = \frac{hD_h}{k}$$

$$Re = \frac{(\dot{m}/A_c)D_h}{\mu}$$

where h is the local heat transfer coefficient; D_h is the hydraulic diameter of the flow passage; k is the thermal conductivity of air; A_w is the surface area of the ellipses; A_c is the minimum flow cross sectional area; L is the total flow length of the intercooler; $\dot{m}$ is the mass flow at the inlet and μ is the dynamic viscosity.

The friction factor f is defined through [10]:

$$\Delta p = \frac{(\dot{m}/A_c)^2}{2\rho_i}\left[f\frac{A_W}{A_c}\frac{\rho_i}{\rho_m} + (1+\sigma^2)\left(\frac{\rho_i}{\rho_o} - 1\right)\right]$$

where Δp is the pressure drop through the intercooler, ρ_i and ρ_o are the fluid inlet and outlet density, ρ_m is the average of ρ_i and ρ_o, σ is the ratio between the minimum flow cross sectional area A_c and the intercooler frontal area A_f.

The correlations provided below are valid in the range of 10,000 < Re < 110,000. The largest deviation from CFD data is 0.90%.

$$j = 0.003469e^{-7.117\times10^{-5}Re} + 0.003461e^{-3.793\times10^{-6}Re}$$

$$f = 0.01044e^{-6.806\times10^{-5}Re} + 0.008109e^{-2.908\times10^{-6}Re}$$

Furthermore, the additional weight and nacelle diameter caused by the intercooler has been considered. Titanium is assumed to be used as intercooler material. The tube thickness is calculated based on the pressure difference between the inner and outer side of the tube. A minimum tube thickness is assumed to be 0.2 mm. The nacelle line moves with the change in intercooler size, in order to keep the external bypass flow Mach number lower than 0.6.

Engine modelling

The advanced non-intercooled geared engine is optimized by varying the bypass ratio, fan, IPC and HPC pressure ratio. The OPR is limited due to the turbine blade and disc cooling temperature, as manifested by a maximum compressor exit temperature of 950 K. The engine take-off net thrust is set to be 65625 lbf which is considered suitable for the twin engine aircraft model used for this study. Design point data and constraints common to the geared and the intercooled geared engine are summarized in Table 2 below. The efficiencies in the table are polytropic. T_{blade} is the allowed maximum blade temperature. A hot day take-off condition is used to evaluate the engine at the start of the mission analysis. The cooling flow is then calculated based on the model established in [14].

Parameter	Value
$T_{HPC,exit}$	< 950 K
$T_{Combustor,exit}$	< 1900 K
T_{blade}	< 1210 K
η_{fan}	93.5%
η_{IPC}	92.2%
η_{HPC}	92.5%
η_{HPT}	90.7%
η_{IPT}	91.4%
η_{LPT}	93.25%
Net Thrust	65625 lbf

Table 2 Design point performance parameters (take-off)

The data presented in Table 2 are based on estimates on performance levels achievable for an engine entering into service year 2020+. The optimization procedure establishes an engine that provides minimum fuel burn for a fixed

mission and fixed aircraft. The mission length is 6800 km. Initial cruise altitude is 35000 ft and final cruise altitude is 39000 ft. A trade factor is established to estimate the full fuel burn saving potential for a scalable aircraft.

With the optimization of the intercooler parameters, the mission study has more design freedom and is more complicated than analysing the advanced non-intercooled engine. The basic intercooler parameters to be determined are the tube diameter, the tube length, the number of rows and number of columns.

The intercooler coolant mass flow is being controlled by a separate variable geometry exhaust nozzle. The exhaust nozzle area is hence included as part of the optimization parameters. Closing the nozzle reduces intercooler external Mach numbers and related pressure losses, both over the intercooler tubes and in the upstream intercooler diffuser. The closing of the nozzle also decreases transferred heat, which leads to an increased combustor inlet temperature and a reduced fuel flow need. The increased compressor power requirement results in an increased turbine inlet temperature and also a somewhat increased temperature in the core exhaust nozzle. In total this process reduces the thermal efficiency but this is outweighed by the strong reduction in irreversibilities generated in the intercooler.

The tube diameter is controlled by the major axis length of the tube, since the aspect ratio is fixed. As the size of the tube is decreasing, the total perimeter length of the tubes increases for a given cross sectional area which leads to an increase of the wetted area.

The tube length, which is set by the radial position of the diffuser and the inner diameter of the internal bypass duct, has the limitation of keeping the external bypass flow Mach number, the nacelle maximum diameter and the internal bypass diffusion loss down. However, an increased tube length gives larger frontal area which in turn gives a lower flow Mach number through the intercooler and hence a lower intercooler external side pressure loss.

Basically, the total heat transfer area is determined by the single tube size and the number of tubes. The number of tubes is equal to the number of tube rows (circumferential direction) multiplied by the number of tube columns (axial direction). The distribution between the number of rows and the number of columns plays an important role in the intercooler performance. Generally, with a given single tube size and heat transfer area, fewer columns are desirable for decreasing the external side pressure loss. A high radius installation of the intercooler gives more rows and fewer columns but also increases the nacelle diameter.

The design parameters determining the basic intercooler parameters are given in Table 3. Here, a is the major axis length of the inside of the elliptical tube, D_i is the hub diameter of the intercooler matrix, D_o is the diameter of the shroud of the intercooler and M_{tube} is the flow Mach number inside the tubes. M_{tube} and a are input to the design process whereas D_i and D_o are obtained from the conceptual design of the engine.

The conceptual design process used here, apart from the intercooler design has been outlined in [11] and is described in more detail in [15, 16]. The weight calculation is integrated in the optimization process and changes for every new

engine/aircraft mission being evaluated.

Basic intercooler parameters	**Design parameters**		
Tube diameter	a		
Tube length	D_i	D_o	
Number of Tube rows	D_i	a	M_{tube}
Number of Tube columns	D_i	a	M_{tube}

Table 3 Intercooler design parameters

Results and Discussions

For the advanced non-intercooled geared turbofan engine, the optimal OPR (take-off) is found to be 61, whereas for the intercooled engine an OPR of 81 is obtained. For the intercooled geared turbofan, a further reduction in mission fuel burn can be achieved for an even higher OPR. However, the minimum compressor blade height constraint of the HPC then becomes active. A rule of thumb is that the compressor blade height should not be lower than 12 mm and the hub tip ratio should be kept lower than 0.92, otherwise, the tip clearance loss and end wall boundary layer losses of the HPC will deteriorate its efficiency.

In order to reduce the number of design parameters, the flow Mach number inside the tubes (M_{tube}) is fixed to be 0.07. This was done after a number of preliminary optimization studies revealed that the optimizer always produced the lowest internal tube Mach number possible. Lower values lead to designs that could not be fitted within the available space constraints. Attempts to increase the external nacelle diameter to accommodate a larger intercooler resulted in an increase in mission fuel burn.

A cruise SFC benefit of 3.2% is observed for the intercooled engine, as seen in Table 4. For the fixed aircraft mission this integrated to a 3.2% fuel burn benefit. The SFC reduction is due to a higher thermal efficiency resulting from a higher OPR and a reduced cooling flow need.

	Advanced non-IC	Intercooled
OPR	61	81
TOC OPR	76	101
Cruise OPR	58	75
BPR	15.42	16.74
Fan PR	1.40	1.44
IPC PR	4.91	4.55
HPC PR	7.72	13.78
HPC last blade height (mm)	19.4	13.6
Take-off HPC exit temperature (K)	941.9	888.4
HPT Cooling bleed ratio	0.19	0.14
Take-off SFC (mg/Ns)	6.28	6.17
TOC SFC (mg/Ns)	13.07	12.93
Cruise SFC (mg/Ns)	13.10	12.68
Cruise $\eta_{thermal}$	0.514	0.524
Cruise $\eta_{propulsive}$	0.823	0.810
a (mm)	NA	30.7
Tube Length (m)	NA	0.37
Rows	NA	11
Columns	NA	20
Intercooler Weight (kg)	NA	309
Engine Weight (kg)	7005	6705
Nacelle Diameter(m)	3.47	3.41
Mission fuel burn (kg)	30425 Base	29440 -3.2%

Table 4 Optimal engine configurations

In addition, the intercooler also contributes to a reduced engine core size through an increase in the specific power of the core,

resulting in an estimated 300 kg weight reduction. The nacelle diameter is only slightly reduced for the intercooled engine contributing only marginally to the reduced fuel burn.

A trade factor was established to take into account that the reduced fuel burn can be used to reduce the aircraft operational empty weight and take-off weight. The trade factor also takes into account that the reduced take-off weight allows for a reduced aircraft drag and a reduced engine thrust. The value of the trade factor was estimated at 1.5 which gives a net fuel burn reduction of 4.8%.

	Take-off	Top of Climb	Mid Cruise
OPR	81	101	75
Core Flow Temperature Drop (K)	87	72	59
Core Pressure loss	3.7%	5.0%	4.6%
Coolant flow Pressure loss	14.5%	10.9%	4.0%
Coolant mass flow (kg/s)	111	38	16
Altitude(ft)	0	35000	39000
Mach number	0	0.81	0.81
Net Thrust (lbf)	66040	15191	8351
$\eta_{thermal}$	0.449	0.531	0.524
$\eta_{propulsive}$	0	0.757	0.810

Table 5 Intercooler operation conditions (Optimal engine configuration)

From Table 5 above it can be seen that the take-off point demands the highest amount of intercooling. For the top-of-climb and cruise points, the heat transfer can be reduced by controlling the separate nozzle to reduce the coolant mass flow. With a lower coolant mass flow, less heat rejection from the core to the external bypass leads to a higher thermal efficiency and propulsive efficiency. Additionally, the flow over the external intercooler surface, which is associated with a relatively high pressure loss, is reduced. This will also add to the improvement of the thermal efficiency.

The minimum mission fuel burn for the intercooled engine is remarkably insensitive to BPR variation as is indicated by Table 6 below. From comparing the cruise point SFC and engine size, the 14.5 BPR engine benefits from lower nacelle drag and engine weight while the higher BPR engine has a greater SFC benefit.

OPR	81	81	81
BPR	14.50	15.50	16.74
Fan PR	1.50	1.48	1.44
IPC PR	4.70	4.59	4.55
a (mm)	29.4	29.0	30.7
Number of tube columns	22	21	20
Tube Length (m)	0.38	0.39	0.37
Nacelle Diameter(m)	3.30	3.34	3.41
Engine Weight (kg)	6385	6438	6705
Cruise SFC (mg/Ns)	12.88	12.78	12.68
$\eta_{thermal}$	0.524	0.525	0.524
$\eta_{propulsive}$	0.797	0.802	0.810
Mission Fuel burn	29555	29449	29440

Table 6 Intercooled configurations for a parametric BPR variation (the last column is the optimal engine)

From BPR 15.5 to 16.74, there is a LPT stage increase due to that the stage loading in the LPT has reached its limit. An additional LPT stage gives a step increase in weight and hence a step increase in fuel burn. However, the reduced FPR implies reduced specific thrust and hence an improved propulsive efficiency. Additionally, as the BPR is increasing, the fan size increases as well as the nacelle

line. This actually gives more space for the intercooler installation and then the intercooler is installed in a higher radial position. As mentioned before, a higher radial position gives fewer columns which are desired for reducing the intercooler pressure losses. The tube length has been reduced as well due to the increased radial position of the intercooler installation. This leads to a reduction in the internal side pressure loss.

The combined effect offsets the weight penalty from the additional LPT stage. The optimal engine is then defined at BPR 16.74. A further increase in BPR will result in an increase in fuel burn due to that the nacelle drag starts to dominate.

Conclusions

In general the two-pass cross flow intercooler has been seen to give a relatively small internal pressure loss. A relatively high external pressure loss has been observed, but this could be limited quite effectively in cruise by the use of the variable exhaust nozzle. The transferred heat with this intercooler concept is relatively modest. It is however sufficient to enable the higher OPR which is restricted by the compressor exit temperatures for the advanced non-intercooled geared engine. An OPR of 75 was achieved in cruise compared to an OPR of 55 for the advanced non-intercooled engine. The intercooled engine OPR is actually higher if the auxiliary nozzle area is kept at its design value, but there is a net gain in fuel burn reduction from reducing its area. The intercooling also allowed for a somewhat smaller engine giving a marginal benefit in nacelle drag reduction and a somewhat larger effect due to a reduced weight. A larger benefit is obtained from the reduced compressor exit temperature which gives a reduced cooling flow need. Potentially the reduced compressor exit temperature could also be used to reduce NO_x emissions.

Acknowledgement

This work is financially supported by the E.U. under the "LEMCOTEC – Low Emissions Core-Engine Technologies", a Collaborative Project co-funded by the European Commission within the Seventh Framework Programme (2007-2013) under the Grant Agreement n° 283216.

We also would like to thank Richard Avellán and Anders Lundbladh at GKN Aerospace, and Andrew Rolt at Rolls-Royce for valuable discussions.

References

[1] Kyprianidis, K., Rolt, A. M., and Grönstedt, T., '*Multi-Disciplinary Analysis of A Geared Fan Intercooled Core Aero-Engine*'. Proceedings of ASME Turbo Expo 2013, San Antonio, Texas, USA, GT2013-95474, June 2013.

[2] Xu, L., Kyprianidis, K., and Grönstedt, T., '*Optimization Study of an Intercooled Recuperated Aero-Engine*'. AIAA Journal of Propulsion and Power, Vol. 29, No.2, pp.424-432, 2013.

[3] Kyprianidis, K., Grönstedt, T., Ogaji, S., Pilidis, P., and Singh, R., 'Assessment of Future Aero-Engine Designs with Intercooled and Intercooled Recuperated Cores', ASME Journal of Engineering for Gas Turbines and Power, 133(1), doi:10.1115/1.4001982 January 2011.

[4] Xu, L. and Grönstedt, T., '*Design and Analysis of an Intercooled Turbofan Engine*'. ASME Journal of Engineering for Gas Turbines and Power, Vol. 132, No. 11, doi:10.1115/1.4000857 Nov 2010.

[5] Grönstedt, T. and Kyprianidis, K., '*Optimizing the Operation of the Intercooled Turbofan Engine'*. Proceedings of ASME Turbo Expo 2010: Power for Land, Sea and Air, Glasgow, UK, ASME GT2010-22519, June 2010.

[6] Rolt, A. M. and Baker, N. J., '*Intercooled Turbofan Engine Design and Technology Research in the EU Framework 6 NEWAC Programme'*. The 19th International Symposium on Air Breathing Engines, Montreal, Canada, ISABE-2009-1278, 2009.

[7] Rolt, A. M. and Kyprianidis, K., *'Assessment of New Aeroengine Core Concepts and Technologies in The EU Framework 6 NEWAC Programme'*. 27th International Congress of The Aeronautical Sciences, Nice, France, ICAS 2010-4.6.3, Sep 2010.

[8] Lundbladh, A. and Sjunnesson, A., '*Heat Exchanger Weight and Efficiency Impact on Jet Engine Transport Applications'*. 16th International Symposium on Air Breathing Engines, Cleveland, Ohio, ISABE-2003-1122, Sep 2003.

[9] Bruner, S., Baber, S., Harris, C., Caldwell, N.,Keding, P., Rahrig, K., Pho, Luck., and Wlezian, N., '*NASA N+3 Subsonic Fixed Wing Silent Efficient Low-Emissions Commercial Transport (SELECT) Vehicle Study*', NASA/CR-2010-216798, Nov, 2010.

[10] Kays, W. M., and London, A. L., *Compact Heat Exchanger*, 2nd ed. McGraw-Hill, ISBN 07-033391-2. 1964.

[11] Xu, L., *'Analysis and Evaluation of Innovatiove Aero Engine Core Concepts*', Ph.D Thesis, Chalmers University of Technology, Sweden, 2011.

[12]Haaland, S. E., '*Simple and Explicit Formulas For the Friction Factor in Turbulent Pipe Flow'*. J.Fluids Eng., 105(1), pp. 89-90. 1983.

[13] Gnielinski, V., '*New Equations for Heat and Mass Transfer in Turbulent Pipe and Channel Flow'*. International Chemical Engineering, 16, pp. 359-368. 1976.

[14] Wilcock, R.C., Young, J.B., and Horlock, J.H., '*The Effect of Turbine Blade Cooling on the Cycle Efficiency of Gas Turbine Power Cycles*'. Journal of Engineering for Gas Turbines and Power, 127, Jan, pp. 109-120, 2005

[15] Grönstedt, T., Au, D., Kyprianidis, K. and Ogaji S., '*Low-Pressure System Component Advancements and Its Influence on Future Turbofan Engine Emissions*', GT2009-60201, ASME Turbo Expo 2009, Florida, Orlando, USA, 2009.

[16] Kyprianidis, K., Au, D., Ogaji, S. and Grönstedt, T., '*Low Pressure System Component Advancements and its Impact on Future Turbofan Engine Emissions*', ISABE-2009-1276, Montreal, Canada, 2009.